Unstructured Grid Technologies for Hydrodynamic Applications with Bodies in Relative Motion and Mesh Deformation

By

Lei Ji

Approved:

Robert V. Wilson Associate Research Professor of Computational Engineering (Director of Dissertation)	Lafayette K. Taylor Research Professor of Computational Engineering (Committee Member)
Steve L. Karman, Jr. Professor of Computational Engineering (Committee Member)	D. Stephen Nichols, III Associate Research Professor of Computational Engineering (Committee Member)
John V. Matthews Assistant Professor of Mathematics (Committee Member)	A. Jerald Ainsworth Dean of the Graduate School

Unstructured Grid Technologies for Hydrodynamic Applications with Bodies in Relative Motion and Mesh Deformation

A Dissertation

Presented for the

Doctor of Philosophy

The University of Tennessee at Chattanooga

Lei Ji

April 2011

Dedication

This dissertation is dedicated to my parents and my sisters, who always support me, inspire me, and encourage me to achieve my goals.

Acknowledgements

First, I would like to thank Dr. Robert Wilson, who always provided plenty of insightful advice and guidance to help me through many challenging problems. Thanks goes to Dr. Kidambi Sreenivas and Dr. Daniel Hyams for helping me during the process of developing the mesh deformation scheme. I would also like to thank Dr. Lafayette Taylor, Dr. Steve Karman, Dr. Stephen Nichols, and Dr. John Matthews for helping me and serving on my graduate committee. Last but not the least, I would like to thank Amy for all her love and support which makes this work possible.

Abstract

Unstructured grid technologies for hydrodynamic applications with bodies in relative motion and mesh deformation are presented. A parallel universal mesh deformation scheme is developed to manage deforming surface and volume grids for both aerodynamic and hydrodynamic applications. The approach is universal and independent of grid type. Also, it requires minimal inter-processor communication and is thus perfectly suitable to a parallel platform. The original scheme of Allen (2006) has difficulty deforming volume grids in regions near concave geometry features and for abrupt grid resolution changes. Several modifications are proposed to overcome these problems. Grid quality can be improved significantly by adding a smoothing algorithm and additional surface mesh connectivity. The mesh deformation scheme is demonstrated and validated by solutions of several synthetic jet test cases from a NASA Langley Workshop. Application to the free surface flow over the S175 container ship undergoing two-node harmonic bending is also demonstrated. The resulting viscous mesh shows good quality throughout the harmonic deformation with large scale vortex shedding occurring at the bow and stern. Overset grids technologies are adopted to simulate the flow past multiple bodies in relative motion. A generalized library DiRTlib and a grid assembly code SUGGAR both developed by Noack (2005) are used to facilitate integration of overset grids method into *Tenasi* flow solver. Both static and dynamic cases are tested. First, for verification, simulation of an oscillating cylinder using overset grids is compared with a baseline configuration using a single grid in rigid

motion (i.e., no relative motion between the cylinder and the farfield), and the solutions agree with each other very well. Then interaction between two oscillating cylinders with same amplitude and frequency but 180-degree phase difference is studied. It is found that significant low pressure is generated between these two cylinders when passing each other at close separation distance. Finally, as the primary motivation for developing simulation capability for modeling the dynamics of interacting platforms, a Suboff passing beneath a container ship is simulated, and satisfactory results are obtained.

Contents

List of Figures

Nomenclature

Symbols:

α	Connection weighting function
α_l	Liquid volume fraction
β	Artificial compressibility factor
Γ	Preconditioning matrix
μ	Viscosity
ϕ	Moving surface weighting functions
ψ	Distance weighting function
ρ	Density
τ_{ij}	Viscous stress tensor
Θ	Velocity component normal to the control volume face
$\vec{n}$	Normal vector
A	Area
a_t	Control volume face velocity

d	Distance between a field point and its neighbor
F	Flux vector
G	Surface flux vector
L	Characteristic length
N	Total residual vector
$nconnect$	Number of connections
nnb	Number of neighbors for a field point
$nsurfaces$	Number of moving surfaces
P	Total pressure
p	Filed point index
Q	Dependent variable vector
R	Spatial residual vector
r	Coordinate vector or ratio of density
S	Gravitational source term vector
sr	Stretching factor
st	Stretching factor
T	Temporal residual vector
t	Time
u	Velocity component in x direction

U_0	Forward speed
u_i	Velocity components
V	Control volume
v	Velocity component in y direction
w	Velocity component in z direction
x_i	Cartesian coordinates

Subscripts:

Ω	Volume integral
$\partial\Omega$	Surface integral
$connect(nc)$	Surface connection point for connection number nc
fs	Free surface property
g	Gas property
l	Liquid property
m	Mixture quantity
nb	Neighbor node number
nc	Connection number
R	Rotation component
T	Translation component
v	Viscous quantity

Superscripts:

$\bar{}$	Roe-averaged quantity
$\hat{}$	Unit vector
$\tilde{}$	Preconditioned quantity
n	n^{th} time level
ns	Surface number

Nondimensional quantities:

μ_m	Viscosity, μ/μ_l
ρ_m	Density, ρ/ρ_l
τ	Time, tU_0/L
Fr	Fround number, $U_0/\sqrt{gL}$
Re_L	Reynolds number, $\rho_l U_0 L/\mu_l$

Chapter 1

INTRODUCTION

1.1 Background

Examples of ship hydrodynamic applications with deforming surfaces include fully coupled fluid-structure interaction (FSI), hull form optimization, controllable pitch propellers, and ship-ship collisions. Simulations of these applications usually demand high quality mesh during the flow solution, which are compounded by the deformation of both surface and volume grids. Additional meshing challenges occur for surfaces with relative motion such as propeller-hull interaction, moving control surfaces, and simulations with multiple and independent bodies.

The U.S. Navy has recently shown a growing interest in faster ships with capability for transoceanic range, high speed operations in high sea states, littoral and stealth operations, rapid deployment, and fast transport of troops and heavy equipment to austere ports (Wilson et al., 2006a). Enormous challenges have been encountered for high fidelity simulations of these applications. Demanding structural designs are required for such ships to withstand both short-term extreme and long-term fatigue loading in high sea states over the lifetime of the vessels. Wave-excited hull vibration can produce significant stress that could cause

damage to the hull body. The most commonly encountered phenomena are known as springing and whipping, respectively. The cause of springing is resonance between the frequency of wave encounter and a natural vibratory frequency of the hull. Calculations suggest that springing may contribute to the extreme response for some ships, but springing vibrations are generally more important for fatigue. It has been found that springing may contribute to about 50% of the accumulated fatigue damage for long bulk carriers (Hermundstad, 2007). Whipping is transient hull girder vibrations due to wave loads that increase rapidly. This will normally be impact loads like those arising from bottom slamming or bow flare slamming. In some wave conditions, a ship may experience slamming loads for almost every wave encounter. Normally, whipping is associated with violent slamming loads in severe wave conditions. The highest hull girder responses are often associated with whipping events. Hence, whipping contributes to the design loads and are very important to assess. For large high speed ships, much effort has been made to reduce the mass of the hull, including the use of lightweight materials such as aluminum, high strength steel, and fiber reinforced plastics. This leads to structures with low rigidity, making them susceptible to structural failure through vertical plane deformation. Operation of ships at higher speeds, where the encounter frequency of the incident wave can match that of the natural two-node vibration frequency, can result in both springing and whipping (Wilson et al., 2008). Cases of severe damage to ship bows due to impact have been reported (Yammamoto et al., 1985). Figure 1.1 is an example of severe ship hull failure due to excessive stresses. The stern of the 153-meter tanker Gem was smashed into two pieces by waves in early March 1962 off the coast of Virginia. Survivors reported that the ship broke in two with a cracking sound. Figure 1.2 is an example of ship capsize. The Greek-registered cargo ship named Ice Prince went down about 26 miles off Portland Bill after being damaged in a storm on January 15, 2008. When Ice Prince sent out its initial emergency call, the waves were reported to be about 16 feet high. As a result, the need for efficient computational tools to predict hydroelastic

responses for high speed ships subjected to large unsteady wave loads is critical.

Ship hydrodynamic simulations also present unique challenges for grid generation due to boundary layer and free surface resolution requirements, complex geometry such as fully appended ships, and large amplitude motions and incident waves. Traditional approaches to gridding complex ship geometries include body-fitted structured grids, which can be tedious, time consuming, and require a non-trivial level of expertise. Recently, there has been increasing need for solving complex problems involving multiple moving bodies in relative motion, such as a store separation, launch and recovery of unmanned vehicles from submarines, ship-ship collision/passing, etc., which are generally more demanding for grid generation and movement.

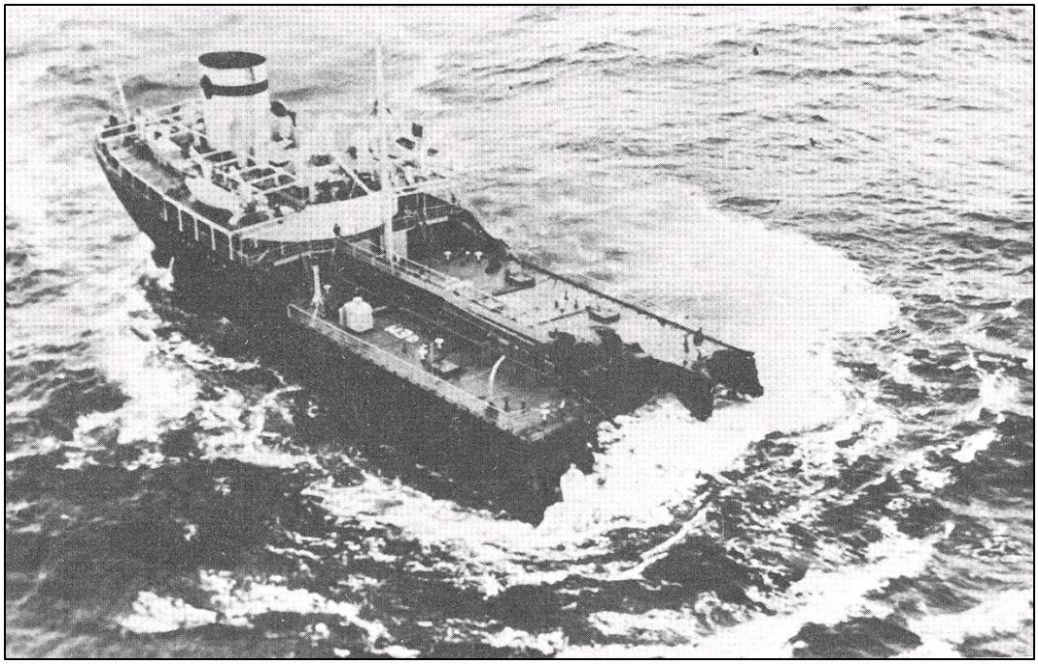

Figure 1.1: A tanker smashed into two pieces by waves (Bishop and Price, 1979)

Figure 1.2: A cargo ship damaged in a storm

1.2 Literature Review

Relevant research progress from other parties has been closely followed during this investigation. Many of the fluid-structure interaction and overset grid topics related papers are from the most recent ONR Symposium on Naval Hydrodynamics (Sep. 2010).

1.2.1 Moving and Deforming Mesh

Many approaches for moving and deforming meshes have been developed previously, which are based on spring analogy or solutions of partial differential equations, but the approach adopted often depends on both the meshing scheme, grid element type, and the proposed application. Originally proposed by Batina (1990), spring analogy was designed to handle some small displacements of the airfoil boundary, although more recently many other researchers have developed this idea to deal with large mesh deformations. It treated each interior edge of the mesh as a spring with certain stiffness. This approach is very expensive and can lead to mesh quality problems for applications with large grid motions. Farhat et al. (1998) extended the spring analogy approach by including a torsional spring to avoid the grid cross over problem. The partial differential equations approach (Löhner and Yang, 1996) usually comes with an elliptic problem solution, which is ideal for small meshes. However, for larger meshes, or for an unsteady simulation where the mesh may needed to be moved at each time step, any spring analogy or elliptic solution method is too expensive. Hence, a cheaper but high quality alternative is needed for the ship hydrodynamic applications that usually come with large grids.

1.2.1.1 Methods for Fluid-Structure Interaction

Traditionally, fluid-structure interaction problems have been studied using potential flow theories for ship motions coupled with modal analysis for structural responses. Among

those potential flow theories, the best known ones are strip theories. They are developed for seakeeping problems (Korven-Kroukovsky and Jacobs, 1957; Salvesen et al., 1970), provide an efficient tool for calculating the hydrodynamic forces acting on a ship hull and formed the essential preliminary step in the establishment of two-dimensional hydroelastic theories for symmetric and antisymmetric responses of hulls (Betts et al., 1977; Bishop and Price, 1977, 1979).

Faltinsen and Zhao (1991a,b) have presented a modified linear strip theory to calculate the seakeeping responses of ship hulls. The three-dimensional Laplace's equation is approximated by a two-dimensional Laplace's equation in the cross-sectional plane but the important wave systems generated by high speed vessels are incorporated properly in the three-dimensional free-surface boundary conditions. Hermundstad et al. (1999) reported that the transverse waves are not incorporated in Faltinsen and Zhao's theory, and therefore, the method is theoretically applicable only to high speed vessels. They presented a linear hydroelastic analysis of high speed vessels based on a modal approach and generalization of Faltinsen and Zhao's theory so that flexible modes can be analyzed in addition to the six rigid modes that are used in conventional seakeeping analysis. Hydrodynamic interaction between the hulls of a catamaran is properly included. An integral theorem was utilized to find the hydrodynamic force for general mode shapes. Based on linear and nonlinear hydroelastic analysis of high speed vessels, Wu and Moan (1996) concluded that the strong nonlinearity is the most prominent feature of high speed vessels even in the moderate sea state and must be taken into account. Various modifications of the linear strip theory approach have been suggested to account for nonlinearities occurring when a ship is sailing in moderate or rough seas (e.g., Jensen and Pedersen, 1979; Jensen and Dogliani, 1996; Xia et al., 1998; Singh and Sen, 2007). However, these approximation approaches suffer from complex ship hull geometry, as well as relatively large motion and velocity, which are usually the sources for nonlinearities. Hence, more systematic validation of these methods are

needed to demonstrate the consistency in the prediction of wave loads, rigid-body motions and structural responses.

For strip theory based methods, added mass and damping coefficients are part of the governing equations. Strip theories assume the flow is irrotational. So in order to take viscous effects into account, they need to be modeled into added mass and damping coefficients. Yang and Moran (1979), along with Huerta and Liu (1988), investigated added mass and damping coefficients of an immersed body oscillating in an incompressible viscous fluid. They both assume that the fluid force is a linear combination of acceleration and velocity and can be expanded using a Fourier series. The term in phase with the acceleration is separated from the one in phase with the velocity. From these two terms, the added mass and damping coefficients can be computed. Journée (1992) gave an analytical solution of added mass and damping coefficients by simplifying the equation for heave and pitch only. Unfortunately, so far no general formula has been developed to calculate these two coefficients with viscous effects.

In the past two decades, modal analysis has become a major technology in the quest for determining, improving, and optimizing dynamic characteristics of engineering structures (He and Fu, 2001). It is the process of determing the inherent dynamic characteristics of a system in forms of natural frequencies, damping factors and mode shapes, and using them to formulate a mathematical model for its dynamic behavior. The dynamics of a structure are physically decomposed by frequency and position. Modal analysis is based upon the fact that the vibration response of a linear time-invariant dynamic system can be expressed as the linear combination of a set of simple harmonic motions called the natural modes of vibration. This concept is akin to the use of a Fourier combination of sine and cosine waves to represent a complicated waveform. The natural modes of vibration are inherent to a dynamic system and are determined completely by its physical properties (mass, stiffness, damping) and their spatial distributions. Each mode is described in terms

of its modal parameters: natural frequency, the modal damping factor and characteristic displacement pattern, namely mode shape. The modal analysis is usually best suited to calculate structural responses. It is often the cheapest way of solving a structural dynamics problem. This is especially true if the effects of several loadings must be studied because the same modes and frequencies are used for each different loading (Cook, 1995).

The question of how to couple computational fluid dynamics (CFD) and computational structural dynamics (CSD) codes has been treated extensively in the literature (e.g., Lee et al., 2008; Wilson et al., 2008; Miller and Kim, 2010). Two main approaches have been pursued to date: strong coupling and loose coupling. The strong (or two-way) coupling technique solves the discrete system of coupled, nonlinear equations resulting from CFD, CSD, and interface conditions in a single step. The loose (or one-way) coupling solves the same system using an iterative strategy, in which the CFD solution is followed by CSD solution until convergence is achieved. Lee et al. (2008) described a simulation process for performing a loosely-coupled fluid-structure interaction simulation on a surface vessel advancing in waves. They used the fully non-linear unstructured viscous CFD solver *Tenasi* to predict the rigid-body motion and surface stress field on the hull and coupled with the commercial finite element solver ABAQUS to perform modal analysis of the hull and the water. More results on this discussion can be found in Wilson et al. (2008). Miller and Kim (2010) proposed a coupling framework that allowed use of any combination of CFD and CSD codes. Effects of moving and deforming solid boundaries were accounted for in CFD solutions using an arbitrary Lagrangian-Eulerian (ALE) technique. Both one-way coupling and two-way coupling simulations were presented.

1.2.1.2 Current Status of RANS Methods

Although most of the studies on ship motions have been based on potential flow codes, recently efforts have been made in using RANS (Reynolds-Averaged Navier-Stokes) method

based codes to solve the problem (Carrica, 2006). Strip theories assume that both the ship and fluid motions are small. They usually underpredict resistance and cannot predict breaking wave and viscous effects (Wilson *et al.*, 2006b). On the other hand, RANS methods have the potential to produce superior results since effects due to viscosity, creation of vorticity in the boundary layer, vortex shedding, and turbulence are naturally included (Wilson et al., 2006c). Applications of RANS methods include resistance/powering, seakeeping, and maneuvering. Resistance is the study of forces opposed to the ship's forward speed. Seakeeping refers to the ship motion response to ocean waves, while maneuvering refers to desired change in ship course due to deflection of control surfaces. Various tests have been carried out to determine the characteristics of ships from these applications. Resistance tests and seakeeping tests are usually carried out in a towing tank, which is a long and narrow basin. In the resistance test, a ship model with a fixed displacement is towed at a constant velocity by a mechanically propelled towing carriage. The resistance of the model at the constant velocity is recorded by the instrument on the carriage. In the seakeeping test, however, the ship model is allowed to move and respond to the incident waves in six degrees of freedom, most commonly as heave, pitch and roll, etc.. Unlike the other two, maneuvering tests are carried out in calm seas by changing the control surface (the rudder) or changing the rate of propeller's rotation. Two kinds of tests are performed most often, namely tactical turns and exact paths. When a ship is advancing on a straight path, if its rudder is deflected and held at a fixed angle, the path of the ship will be circular. This is called tactical turn. It has been and still is an important practical maneuver that ships frequently perform. It is also important that the ship can perform the exact test, in which a ship usually travels in a precalculated desired path, such as a spiral path. A series of international workshops held in the past on the application of RANS methods have focused mainly on steady free surface flow for resistance and powering (Larson et al., 2002; Larson et al., 2003; Hino, 2005). Those approaches are now being applied to seakeeping and

maneuvering as well. Examples of RANS applications to seakeeping in the literature can be found in Hochbaum and Vogt (2002), Orihara and Miyata (2003), Carrica *et al.* (2007), and Wilson et al. (2006c), while application for unsteady maneuvering can be found in Hochbaum (2006), Wilson et al. (2007), and Broglia et al. (2006). Broglia and Iafrati (2010) simulated the flow generated by a wedge shaped hull planing in steady conditions at a constant trim angle by means of a RANS equation model and used different values of the heel angle to achieve a better comprehension of the changes induced by the rotation. More applications of RANS method can be found in Wilson's technical report (Wilson, 2008).

1.2.2 Multiple Moving Bodies in Relative Motion

The simulation of flow past multiple moving bodies in relative motion is a challenging task due to the presence of complex geometries and flow features, moving grids, and rigid body movements under the action of external forces and moments. Constructing a good quality single-block, structured, curvilinear mesh for complex geometries is often formidable. Algorithms employing unstructured grids provide a powerful alternative for simulating flows in arbitrarily complex geometries and have been successfully applied to a number of complex compressible and incompressible flows (Ramamurti et al., 1999; Wilson et al., 2006a-2006c, 2007). Unstructured grids facilitate grid generation in complex domains and allow for the relatively easy implementation of locally adaptive algorithms. Such methods, however, could be memory and computational time intensive compared to structured grid methods. Moreover, generating a fully unstructured grid near solid boundaries in high Reynolds-number flow simulations is far from trivial. In fact, most available unstructured algorithms have to resort to locally structured or prism layer grids to accurately resolve near-wall boundary layers.

An alternative to unstructured grids is the so-called composite, overset grid approach pioneered by Benek *et al.* (1983). The overset (also known as overlapping) grid methodol-

ogy is a mature technology that has been used for many years to simplify the structured grid generation requirements for complex geometries. It decomposes complex geometrical configuration into a set of simpler, overlapping subdomains, each designed so that it can be easily discretized with a set of simple, boundary-conforming, curvilinear coordinates. Compared to their unstructured grid counterparts, composite structured grid algorithms are worth pursuing because they: (1) lead to more efficient numerical algorithms; (2) simplify the implementation of high-resolution discretization schemes; and (3) allow for efficient clustering of grid surfaces near solid walls, thus enhancing accuracy in high Reynolds-number simulations.

The accurate characterization of the flow features in the stern region of a ship is a complex task that has driven a rising interest in detailed numerical tools to be used for both new design approaches as well as to get a better insight into the complex mechanism of interaction among the propeller slipstream, the hull, and the rudder. Muscari et al. (2010) investigated the flow around a propeller behind a fully appended hull through both experimentation and integration of the unsteady RANS equations. A dynamic overlapping grid approach was used to take into account the real geometry of the propeller. The flow field was analyzed, and the results from the two approaches were compared and showed good agreement. Durant et al. (2010) performed 6DOF simulation of the turning circle maneuver for a tanker-like ship model in its fully appended configuration. Complex geometries and multiple bodies (i.e. propellers and rudder) in relative motion were handled by a suitable dynamical overlapping grid approach. The maneuver results were compared with experimental data from free running tests carried out at the Nemi Lake, and the agreement was satisfactory.

Many overset grid assembly codes have been used over the years. The mainstay for the assembly of structured grids has been the PEGASUS family of codes (Suhs et al., 2002). The PEGASUS codes are separate from the flow solver and have been used for both static and, by

using scripts, moving body simulations. In fact, the predominant implementation of overset methodology over the past decade has been in structured grid flow solvers. The primary disadvantage of this approach is the difficulty in generating structured, hexahedral grids around complex unconventional geometries. In recent years, the overset grid technology has begun to migrate into unstructured grid flow solvers (Madrane et al., 2004). The prime advantage of using unstructured grids is the relative ease of generating tetrahedral grids about complex geometries, which can take hours or days. Thus, unstructured overset-grid codes offer the hope of more rapid response to flow problems with multi-component motion. Atsavapranee et al. (2010) conducted steady-turning experiments and RANS simulations using URANS solver CFDShip-Iowa on a surface combatant. They showed that overset grids are useful for "stripping" type simulations where appendages are added or removed to match the test configuration. The Structured, Unstructured and Generalized Grid AssembleR (SUGGAR) code (Noack, 2005b) was used in CFDShip-Iowa to perform grid assembly of the component grids, such as hull orientation and rudder deflections. Both experimental and numerical simulations provided physical insights into the complex flow interaction between the hull and various appendages and the propellers.

Another approach for overset methodology is based on a local distance function. Several independent groups have been working on this method. Nakahashi *et al.* (2000) used unstructured grids for multiple moving-body aeronautical problems. Regnström and Bathfield (2006) used structured grids for local refinements around the hull and its appendages in marine applications. Recently, Orych *et al.* (2010) proposed some adaptive overlapping grid techniques and spatial discretization schemes for increasing surface sharpness and numerical accuracy in free surface capturing methods.

1.3 Objective and Approach

The objective of this investigation is to develop next-generation technology for complex unsteady RANS simulations including FSI and interaction between multiple bodies.

A novel approach called algebraic interpolation method proposed by Allen (2006) is followed in this work. It is based on a global parameterization without the requirement of local connectivity data. This implies that the scheme is universal for any grid type and perfectly suitable to a parallel platform. However, the original method is designed for purely rotational mesh movement, which cannot handle our two-node bending applications. Thus, some improvements have been made to meet the new challenge.

The overset grid approach is adopted to handle moving bodies problems. The overset composite grids utilize a set of overlapping grids to discretize the domain and use interpolation at appropriate points to couple the solution on the different grids. Any points that lie outside the domain of interest, for example inside of a body or behind a symmetry plane, are marked for exclusion from the computations and are termed "hole points". Points that surround the hole points become new inter-grid boundary points, which are called fringe or receptor points, and require boundary values to be applied. The boundary values required by a receptor point are provided by interpolating from a donor grid that overlaps the region. The overset grid assembly process provides the domain connectivity information, which is the definition of which points are receptor points along with their corresponding donor members and which are hole points.

The implementation of overset grids technique into existing structured and unstructured flow solvers typically requires extensive and tedious code modifications. The modifications enable highly integrated functions of hole cutting, surface-grid assembly, near-body grid assembly, and off-body grid assembly. Since most of the overset functions are straightforward and essentially duplicated among flow solvers, Noack (2005a) developed a powerful set of

tools, called Donor interpolation Receptor Transaction library (DiRTlib), and the Structured, Unstructured and Generalized Grid AssembleR (SUGGAR) code (Noack, 2005b), to facilitate the rapid implementation of overset grid capability into most structured flow solvers. Experience has shown that this capability can be installed into most flow solvers within days. The successful integration of SUGGAR into existing flow solvers has been reported in many publications (Pandya *et al.*, 2005; Koomullil *et al.*, 2008; Atsavapranee *et al.*, 2010; Dreyer and Boger, 2010)

The present investigation describes the implementation of the DiRTlib functional libraries and SUGGAR into the SimCenter's in-house viscous flow solver, *Tenasi*, to create an overset grid capability in an established unstructured flow solver.

1.4 Present Contribution

Unstructured grid technologies are developed and implemented into the *Tenasi* flow solver to manage complex unsteady simulations for deforming grids and relative motions. These technologies are added to meet the SimCenter project requirements allowing simulations for objects with large relative motion and close proximity.

Algebraic Interpolation Method (AIM) with improvement is developed to to manage deforming surface and volume grids for both aerodynamic and hydrodynamic applications. The approach is universal and independent of grid type; structured or unstructured. Also, it requires minimal inter-processor communication and is thus perfectly suitable to a parallel platform.

The original scheme of Allen (2006) has difficulty deforming volume grids in regions near concave geometry features and for abrupt grid resolution changes. Several modifications are proposed to overcome these problems. Grid quality can be improved significantly by adding a smoothing algorithm and additional surface mesh connectivity. The mesh deformation

scheme is demonstrated and validated by solutions of several synthetic jet test cases from a NASA Langley Workshop. Application to the free surface flow over the S175 container ship undergoing two-node harmonic bending was also demonstrated. The resulting viscous mesh shows good quality throughout the harmonic deformation with large scale vortex shedding occurring at the bow and stern.

Overset grids technologies are adopted to simulate the flow past multiple bodies in relative motion. A generalized library DiRTlib and a grid assembly code SUGGAR both developed by Noack (2005) are used to facilitate integration of overset grid method into *Tenasi* flow solver. First, for verification, simulation of an oscillating cylinder using overset grids is compared with a baseline configuration using a single grid in rigid motion (i.e., no relative motion between the cylinder and the farfield), and the solutions agree with each other very well. Then interaction between two oscillating cylinders with same amplitude and frequency but 180-degree phase difference is studied. Finally, as the primary motivation for developing simulation capability for modeling the dynamics of interacting platforms, a Suboff passing beneath a container ship is simulated using both 2D and 3D overset grids, and satisfactory results are obtained.

Chapter 2

GOVERNING EQUATIONS

2.1 Flow Equations

The governing equations are presented here for two incompressible and immiscible phases (i.e., a liquid and gas). Following Chorin (1967), an artificial compressibility approach is used to couple velocity and pressure and to cast the set of equations into a time marching form (Hyams, 2000). A multiphase free surface capturing technique is implemented to overcome limitations associated with surface tracking approaches and to manage complex interfacial topologies such as steep and overturning waves associated with high Froude number and/or large amplitude ship motions and maneuvers (Nichols, 2002).

Using these approaches, the nondimensional incompressible continuity, Reynolds-averaged Navier-Stokes momentum equations, and nonconservative transport of the liquid volume fraction α_l are given in primitive variable form by

$$\frac{1}{\rho_m \beta}\frac{\partial}{\partial \tau}\left(P + \frac{\rho_m y}{Fr^2}\right) + \frac{\partial u_i}{\partial x_i} = 0 \tag{2.1}$$

$$\rho_m \frac{\partial u_i}{\partial \tau} + \frac{\partial \left(\rho_m u_i u_j\right)}{\partial x_j} + u_i \Delta_\rho \frac{\partial \alpha_l}{\partial \tau} = -\frac{\partial P}{\partial x_i} + \frac{1}{Re_L}\frac{\partial \tau_{ij}}{\partial x_j} - \frac{\rho_m}{Fr^2}\frac{\partial x_2}{\partial x_i} \tag{2.2}$$

$$\frac{\partial \alpha_l}{\partial \tau} + \frac{\partial \left(\alpha_l u_j\right)}{\partial x_j} + \frac{\alpha_l}{\rho_m \beta} \frac{\partial}{\partial \tau} \left(P + \frac{\rho_m y}{Fr^2} \right) = 0 \tag{2.3}$$

The variables $x_i = x, y, z$ and $u_i = u, v, w$ are the Cartesian cooridnates and velocity components, respectively. Variables are nondimensionalized with the characteristic length (L), forward speed (U_0), and the nondimensional total pressure (i.e., it has both dynamic and hydrostatic components) is given by $p = (p^* - p_0)/\rho_l U_0^2$. Notice that an extra component ($\rho_m y/Fr^2$) has been added to the pressure time derivative in the continuity equation (2.1) and volume fraction equation (2.3). Experience has shown that the addition of the extra component greatly improves convergence of the pressure and does not effect the final solution since the fictitious time derivative vanishes upon convergence. Liquid properties are used to define a nondimensional density ($\rho_m = \rho/\rho_l$) and viscosity ($\mu_m = \mu/\mu_l$) and β is the artificial compressibility factor (a value of 15 is used here). The liquid volume fraction α_l is used to define nondimensional density and viscosity mixture properties from constituent values

$$\rho_m = r_\rho + (1 - r_\rho)\alpha_l = r_\rho + \Delta_\rho \alpha_l \tag{2.4}$$

$$\mu_m = r_\mu + (1 - r_\mu)\alpha_l = r_\mu + \Delta_\mu \alpha_l \tag{2.5}$$

where $r_\rho = \rho_g/\rho_l$ and $\Delta_\rho = 1 - r_\rho$, with similar definitions for viscosity. The Reynolds and Froude numbers are given by $Re_L = \rho_l U_0 L/\mu_l$ and $Fr = U_0/\sqrt{gL}$, where the gravity vector is aligned with the y coordinate direction. The turbulent stresses are modeled using an eddy viscosity approach, so that the viscous stress tensor is given by

$$\tau_{ij} = (\mu_m + \mu_t) \left(\frac{\partial u_i}{\partial x_j} + \frac{\partial u_j}{\partial x_i} \right) \tag{2.6}$$

The total pressure P in equations (2.1)-(2.3) can be decomposed as follows

$$P = p^* - \frac{\rho_m \Delta y_{fs}}{Fr^2} \tag{2.7}$$

where $\Delta y_{fs} = y - y_{fs}$ is the vertical offset between the point x, y, z and its nearest point on the free surface (in terms of total distance) x_{fs}, y_{fs}, z_{fs}, and thus the last term in equation (2.7) represents the hydrostatic pressure difference with respect to the closest free surface point. Substituting equation (2.7) into (2.1)-(2.3) yields

$$\frac{1}{\rho_m}\frac{\partial p^*}{\partial \tau} + \frac{\zeta}{\rho_m}\frac{\partial \alpha_l}{\partial \tau} + \frac{\partial \beta u_i}{\partial x_i} = 0 \tag{2.8}$$

$$\rho_m \frac{\partial u_i}{\partial \tau} + \frac{\partial \left(\rho_m u_i u_j\right)}{\partial x_j} + u_i \Delta_\rho \frac{\partial \alpha_l}{\partial \tau} = -\frac{\partial p^*}{\partial x_i} + \frac{\partial}{\partial x_i}\left(\frac{\rho_m \Delta y_{fs}}{Fr^2}\right) + \frac{1}{Re_L}\frac{\partial \tau_{ij}}{\partial x_j} - \frac{\rho_m}{Fr^2}\frac{\partial x_2}{\partial x_i} \tag{2.9}$$

$$\left(\beta + \frac{\zeta \alpha_l}{\rho_m}\right)\frac{\partial \alpha_l}{\partial \tau} + \beta \frac{\partial \alpha_l u_j}{\partial x_j} + \frac{\alpha_l}{\rho_m}\frac{\partial p^*}{\partial \tau} = 0 \tag{2.10}$$

where $\zeta = \Delta\rho y_{fs}/Fr^2$. The set of coupled equations for conservation of mass, momentum, and the liquid volume fraction in integral form are then given by

$$\Gamma \frac{\partial}{\partial t}\int_\Omega Q dV + \int_{\partial\Omega} \vec{F}\cdot\vec{n} dA = \frac{1}{Re_L}\int_{\partial\Omega} \vec{F}_v \cdot \vec{n} dA + \int_{\partial\Omega} \vec{G}\cdot\vec{n} dA + \int_\Omega \vec{S} dV \tag{2.11}$$

where $\vec{n} = n_x\hat{i} + n_y\hat{j} + n_z\hat{k}$ is the outward pointing normal vector to the control volume V and where surface and volume integrals are used to convert the third and fourth terms, respectively, on the RHS of equation (2.9) to integral form. The vector of dependent variables (Q) and the inviscid flux ($\vec{F}\cdot\vec{n}$), viscous flux ($\vec{F}_v\cdot\vec{n}$), surface flux ($\vec{G}\cdot\vec{n}$) and

volume source ($\vec{S}$) vectors are given by

$$Q = \begin{bmatrix} p^* \\ u \\ v \\ w \\ \alpha_l \end{bmatrix} \tag{2.12}$$

$$\vec{F} \cdot \vec{n} = \begin{bmatrix} \beta(\Theta - a_t) \\ \rho_m u\Theta + n_x p^* \\ \rho_m v\Theta + n_y p^* \\ \rho_m w\Theta + n_z p^* \\ \alpha_l \beta\Theta \end{bmatrix} \tag{2.13}$$

$$\vec{F_v} \cdot \vec{n} = \begin{bmatrix} 0 \\ n_x\tau_{xx} + n_y\tau_{xy} + n_z\tau_{xz} \\ n_x\tau_{yx} + n_y\tau_{yy} + n_z\tau_{yz} \\ n_x\tau_{zx} + n_y\tau_{zy} + n_z\tau_{zz} \\ 0 \end{bmatrix} \tag{2.14}$$

$$\vec{G} \cdot \vec{n} = \frac{\rho_m \Delta y_{fs}}{Fr^2} \begin{bmatrix} 0 \\ n_x \\ n_y \\ n_z \\ 0 \end{bmatrix} \tag{2.15}$$

$$\vec{S} = \begin{bmatrix} 0 \\ 0 \\ -\frac{\rho_m}{Fr^2} \\ 0 \\ 0 \end{bmatrix} \tag{2.16}$$

The velocity component normal to the control volume face is defined as

$$\Theta = n_x u + n_y v + n_z w + a_t \tag{2.17}$$

where $a_t = -(V_x\hat{i} + V_y\hat{j} + V_z\hat{k})$ is the control volume face velocity. The preconditioning matrix is given by

$$\Gamma = \begin{bmatrix} \frac{1}{\rho_m} & 0 & 0 & 0 & \frac{\zeta}{\rho_m} \\ 0 & \rho_m & 0 & 0 & u\Delta_\rho \\ 0 & 0 & \rho_m & 0 & v\Delta_\rho \\ 0 & 0 & 0 & \rho_m & w\Delta_\rho \\ \frac{\alpha_l}{\rho_m} & 0 & 0 & 0 & \frac{\zeta\alpha_l}{\rho_m} + \beta \end{bmatrix} \tag{2.18}$$

where $\Delta_\rho = 1 - r_\rho$.

Chapter 3

NUMERICAL METHOD

3.1 Numerical Method for Flow Simulation

The presentation of the numerical method for flow simulation roughly follows that given in Hyams (2000). The set of governing equations, equation (2.11) can be expressed as

$$N = \Gamma T + R = 0 \tag{3.1}$$

where

$$T = \frac{\partial}{\partial t} \int_{\Omega} Q dv \tag{3.2}$$

$$R = \int_{\partial\Omega} \left(\vec{F} - \frac{1}{Re_L} \vec{F_v} - \vec{G} \right) \cdot \vec{n} dA - \int_{\Omega} \vec{S} dV. \tag{3.3}$$

The total residual denoted by N has temporal and spatial components given by T and R respectively.

3.1.1 Spatial Residual

The surface integrals are discretized using a finite volume technique by summing the fluxes through each of the faces of the control volume

$$R = \sum_{i=1}^{k} \left(\vec{F} - \frac{1}{Re_L} \vec{F_v} - \vec{G} \right)_i \cdot \vec{n}_i A_i \tag{3.4}$$

where k denotes the number of faces on the control volume and A denotes the area of the face.

The dependent variables are located at the vertices while the residual calculations shown in equation (3.4) are conducted at the faces of the control volume. Higher order flux evaluations are achieved by extrapolating the solution at the vertices to the faces by

$$Q_i = Q + \vec{\nabla} Q \cdot \vec{r}_i \tag{3.5}$$

where $\hat{r_i}$ is a vector from the vertex to face i. The unweighted least squares method (solved via QR factorization; Anderson and Bonhaus, 1994) is used to compute the gradients for the extrapolation to evaluate the inviscid flux.

The evaluation of the discrete residual is performed separately for the inviscid and viscous terms given in equation (2.11). The Roe Scheme (Roe, 1981) is used to evaluate the inviscid fluxes at the face of the control volume. The algebraic flux vector is replaced by a numerical flux function, which depends on the reconstructured data on each side of the control volume face. Allowing ϕ to denote the flux through a face and $F = \vec{F} \cdot \vec{n}$ gives

$$\phi = \frac{(F_L + F_R)}{2} - \frac{1}{1} \hat{\Gamma} \left| \bar{\tilde{A}} \right| (Q_A - Q_L) \tag{3.6}$$

where $\tilde{A} = \Gamma^{-1} A$ and $A = \partial F / \partial Q$ is the inviscid flux Jacobian. Note that $\bar{\tilde{A}}$ is evaluated

with Roe-averaged variables, which is simply the arithmetic average between left and right solution states in the case of incompressible flow (Taylor, 1991).

For the general element grids used in this study, it is expedient to use only edge-local information to compute the viscous fluxes. This allows the evaluation of viscous fluxes on each face of the control volume without regard to the varying element types of the mesh. The viscous fluxes are evaluated directly at each edge midpoint using separate approximations for the normal and tangential components of the gradient vector to construct the velocity derivatives. Following Hyams (2000), a directional derivative along the edge (i-j) to approximate the tangential component of the gradient leads to the following expression:

$$\nabla Q_{ij} \approx \overline{\nabla Q} + \left[Q_j - Q_i - \overline{\nabla Q} \cdot \overrightarrow{\Delta s} \right] \frac{\overrightarrow{\Delta s}}{\left| \overrightarrow{\Delta s} \right|^2} \tag{3.7}$$

The weighted least squares method is used to evaluate the nodal gradients for the viscous flux.

3.1.2 Temporal Residual

A finite difference expression to approximate the time derivative term appearing in equation (3.1) is given by

$$\Delta q^n = \frac{\Delta t}{1+\theta} \frac{\partial}{\partial t}(q^{n+1}) + \frac{\theta}{1+\theta} \Delta q^{n-1} \tag{3.8}$$

where $\Delta q^n = q^{n+1} - q^n$. A first order accurate in time Euler implicit scheme is given by $\theta = 0$, and a second order time accurate Euler implicit scheme is given by $\theta = 1/2$.

The temporal component of the residual can be expressed as

$$T = \frac{\partial q}{\partial t} \approx \frac{\Delta q}{\Delta t} \tag{3.9}$$

where $q = \int Q dv$. Recalling equation (3.1) gives

$$\Delta q^n - \frac{\theta}{1+\theta}\Delta q^{n-1} = -\Gamma^{-1}\frac{\Delta t}{1+\theta}R^{n+1} \tag{3.10}$$

For the purpose of evaluating volume integrals, the solution variables are assumed to be constant throughout the cell. As such, $q = QV$ and

$$\Delta q^n = V^{n+1}\Delta Q^n + Q^n \Delta V^n \tag{3.11}$$

$$\Delta q^{n-1} = V^{n-1}\Delta Q^{n-1} + Q^n \Delta V^{n-1} \tag{3.12}$$

Now equation (3.10) can be written as

$$V^{n+1}\Delta Q - \frac{\theta}{1+\theta}V^{n-1}\Delta Q^{n-1} + Q^n\left[\Delta V^n - \frac{\theta}{1+\theta}\Delta V^{n-1}\right] + \Gamma^{-1}\frac{\Delta t}{1+\theta}R^{n+1} = 0 \tag{3.13}$$

One must consider the Geometric Conservation Law (GCL). This statement relates the rate of change of a physical volume to the motion of the volume faces

$$\frac{\partial V}{\partial t} = \int_\Omega \nabla \cdot \vec{V}_s dV = \int_{\partial\Omega} \vec{V}_s \cdot \hat{\vec{n}} dA \tag{3.14}$$

The solution of the volume conservation equation must be performed in exactly the same manner as the flow equations to ensure the GCL is satisfied. This procedure ensures that spurious source terms caused by volume changes are eliminated. Using the same time differencing expression, equation (3.8), to approximate equation (3.14) gives

$$\Delta V^n - \frac{\theta}{1+\theta}\Delta V^{n-1} = \frac{\Delta t}{1+\theta}R^{n+1}_{GCL} \tag{3.15}$$

where $R^{n+1}_{GCL} = \sum_{i\epsilon N(0)} \vec{V}^{n+1}_{s,0i} \cdot \vec{n}^{n+1}_{0i}$.

Note that the left hand side of the preceding equation is exactly the bracketed term in equation (3.13). Replacing the bracketed term and rearranging slightly gives the final form of the discretization of the time derivative

$$\Gamma \left[\frac{(1+\theta)V^{n+1}\Delta Q^{n} - \theta V^{n-1}\Delta Q^{n-1}}{\Delta t} + Q_n R_{GCL}^{n+1} \right] + R^{n+1} = 0 \tag{3.16}$$

For incompressible flows, it is prudent to ensure a divergence-free velocity field at the end of each Newton iteration. To this end, the contribution of the time derivative and GCL terms to the residual are removed for the continuity equation only.

3.1.3 Time Evolution

Equation (3.16) needs to be solved at the $n+1$ time level and, recalling equation (3.1), may be expressed as

$$N^{n+1} = 0 \tag{3.17}$$

However, the solution at the $n+1$ time level is unknown. Thus, equation (3.17) is linearized by Newton's method about the known solution Q^n. This linearization is given by

$$\frac{\partial N^{n+1,m}}{\partial Q}\Delta Q^{n+1,m} = -N^{n+1,m} \tag{3.18}$$

$$\Delta Q^{n+1,m} = Q^{n+1,m+1} - Q^{n+1,m} \tag{3.19}$$

Equation (3.18) is iterated until the desired level of convergence is achieved. To start the process, $Q^{n+1,0} = Q^n$ is chosen. For steady state simulation, a single iteration of equation (3.18) is performed at each time step. For unsteady simulation, three to five Newton iterations are performed at each time step to ensure adequate temporal convergence.

3.1.4 Boundary Condition

Viscous conditions are enforced by modifying the linear system such that the no-slip velocity boundary condition is enforced and the pressure is driven according to the imbalance in the continuity equation in the boundary control volume (Anderson and Bonhaus, 1994). Farfield conditions are handled via a characteristic variable reconstruction; all boundary conditions are handled in an implicit fashion. Symmetry plane boundary conditions impose $\nabla\Psi \cdot \vec{b} = 0$ for solution variables. In addition, no flow is allowed through the symmetry plane.

Chapter 4

Algebraic Interpolation Method

4.1 Mesh Deformation: Algebraic Interpolation Method Equations

The algebraic interpolation method (AIM) was originally produced by Allen (2006) for numerical simulation for rotors in forward flight, including cyclic deformation of helicopter blades. With the AIM, the domain is classified into moving and non-moving boundaries. The geometry of the moving surfaces can be either prescribed as a function of time or computed during the flow solution. At each internal field point, a distance function is defined using all the boundaries. A search is employed to find the closest points on each surface and a geometric argument is used to define the weighting of each of these connections.

The original AIM approach by Allen (2006) is summarized below. For a field point p, the displacement between the undisturbed grid point position vector r^p and the deformed position vector $r^p(t)$ at any time t can be evaluated algebraically as a weighted combination of a translation vector $\Delta r_T^{p,ns}$ and a rotation vector $\Delta r_R^{p,ns}$

$$r^p(t) = r^p + \sum_{ns=1}^{nsurfaces} \left(\Delta r_T^{p,ns} \left(1.0 - \psi^{p,ns}\right)^{st} + \Delta r_R^{p,ns} \left(1.0 - \psi^{p,ns}\right)^{sr} \right) \tag{4.1}$$

$$\Delta r_T^{p,ns} = \sum_{nc=1}^{nconnect} \alpha_{nc}^{p,ns} \Delta r_{connect(nc)}^{p,ns} \tag{4.2}$$

$$\Delta r_R^{p,ns} = [R^{p,ns} - I] \left(r^p - \sum_{nc=1}^{nconnect} \alpha_{nc}^{p,ns} r_{connect(nc)}^{p,ns} \right) \tag{4.3}$$

where $nsurfaces$ is the number of moving surfaces. $nconnect$ is the number of connections per moving surface. $\alpha_{nc}^{p,ns}$ is the geometry weighting factor for each connection. $\phi^{p,ns}$ is the surface connectivity weighting function. $\psi^{p,ns}$ is the relative distance function at point p relative to each surface ns, and $r_{connect(nc)}^{p,ns}$ is the position vector of connection point nc on surface ns. The parameters st and sr are prescribed constants in the original method and refer to the scaling exponent of the translation and rotational components, which controls how far these displacements propagate into the mesh. Typical values for these exponents are between 2 and 5.

The distance function $\psi^{p,ns}$ at each point p corresponding to each moving surface ns is defined as

$$\psi^{p,ns} = S^{p,ns} / \left(S_F^p + S^{p,ns} \right) \tag{4.4}$$

where

$$\begin{aligned}
S_{nc}^{p,ns} &= \left| r^p - r_{connect(nc)}^{p,ns} \right| \\
S_F^p &= \left| r^p - r_{farfield}^p \right| \\
0 &\leq \alpha_{nc}^{p,ns} \leq 1 \\
S^{p,ns} &= \sum_{nc=1}^{nconnect} \alpha_{nc}^{p,ns} S_{nc}^{p,ns} \qquad nc = 1, ..., nsurfaces \\
\sum_{nc=1}^{nconnect} \alpha_{nc}^{p,ns} &= 1 \qquad nc = 1, ..., nsurfaces
\end{aligned}$$

Figure 4.1 and 4.2 display the distance function countour of a NACA0012 airfoil, with global and local concentration respectively.

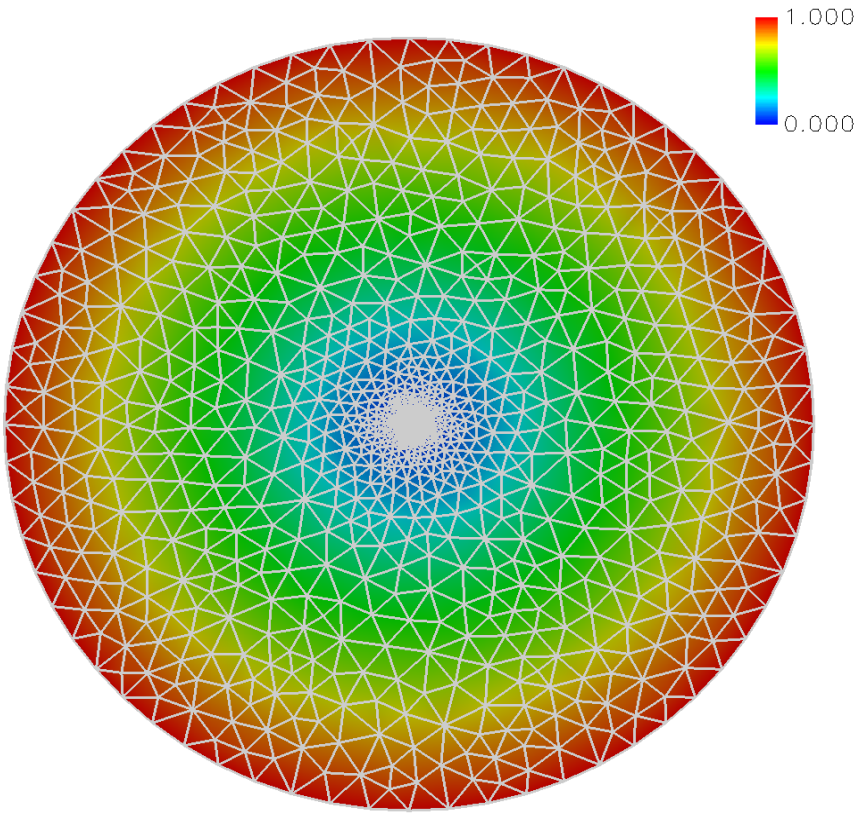

Figure 4.1: Distance function of the NACA0012 airfoil (global)

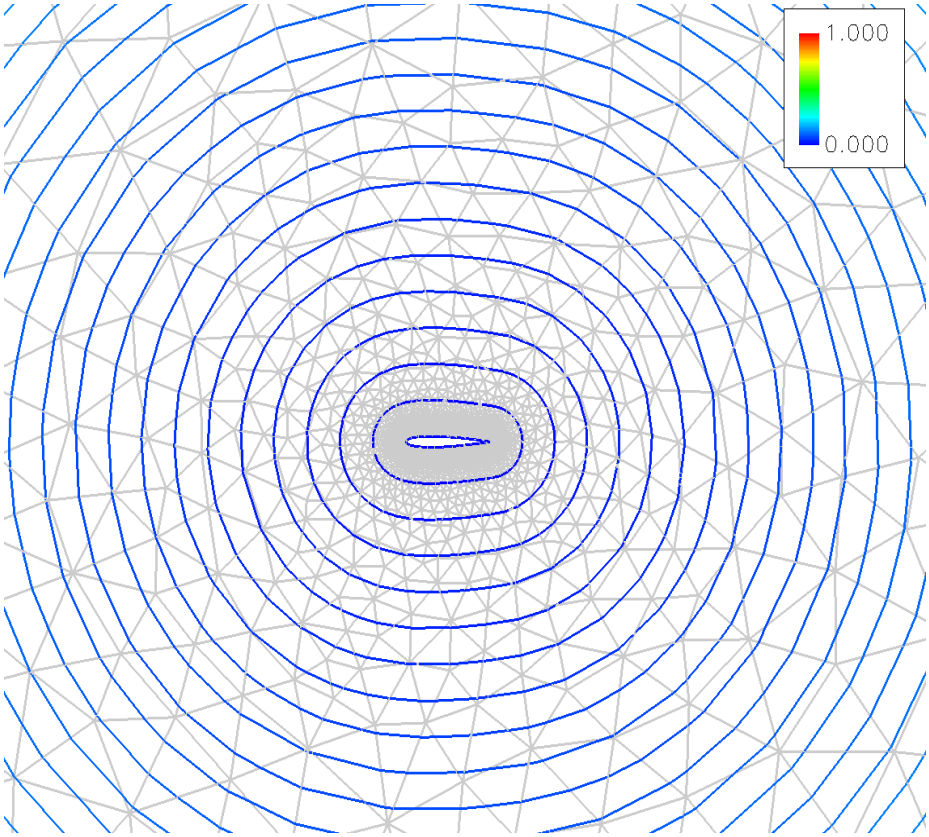

Figure 4.2: Distance function of the NACA0012 airfoil (close-up of local airfoil)

For cases with multiple moving surfaces, a weighting function is used to determine the amount of motion contributed from each surface. The closest surface is found and then the relative distance to each surface found for each point p by

$$S^p_{min} = MIN(S^{p,1}, S^{p,2}, ..., S^{p,nsurfaces}) \tag{4.5}$$

$$S^{p,ns}_{surface} = S^p_{min}/S^{p,ns} \tag{4.6}$$

$$S^p_{Total} = \sum_{ns=1}^{nsurfaces} \left(S^{p,ns}_{surface}\right)^{SSC} \tag{4.7}$$

With the above quantities, the weighting functions are then defined as

$$\phi^{p,ns} = S^{p,ns}_{surface}/S^p_{Total} \tag{4.8}$$

$[R^{p,ns}]$ is the rotation matrix of the surface connection points on surface ns associated with the field point p, and $[I]$ is the identity matrix. Depending on whether it is 2D or 3D problem, $[R^{p,ns}]$ can have different form. In two dimensions,

$$\theta^{p,ns} = \sum_{nc=1}^{nconnect} \alpha^{p,ns}_{nc}\theta^{p,ns}_{connect(nc)} \tag{4.9}$$

$$[R^{p,ns}] = \begin{bmatrix} \cos\theta^{p,ns} & \sin\theta^{p,ns} \\ -\sin\theta^{p,ns} & \cos\theta^{p,ns} \end{bmatrix} \tag{4.10}$$

Figure 4.3-4.5 describe what weighting functions look like for a 3-element airfoil on each individual part: slat, main element, and flap respectively.

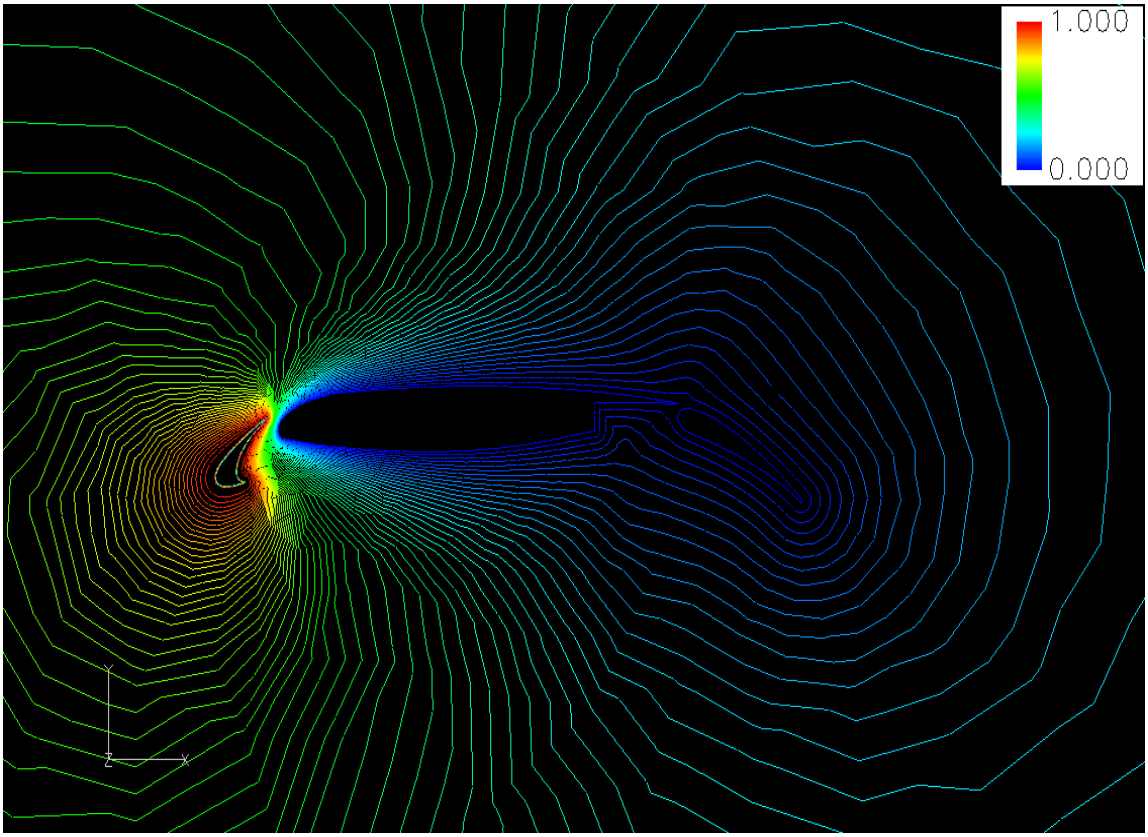

Figure 4.3: Weighting function of 3-element airfoil (slat)

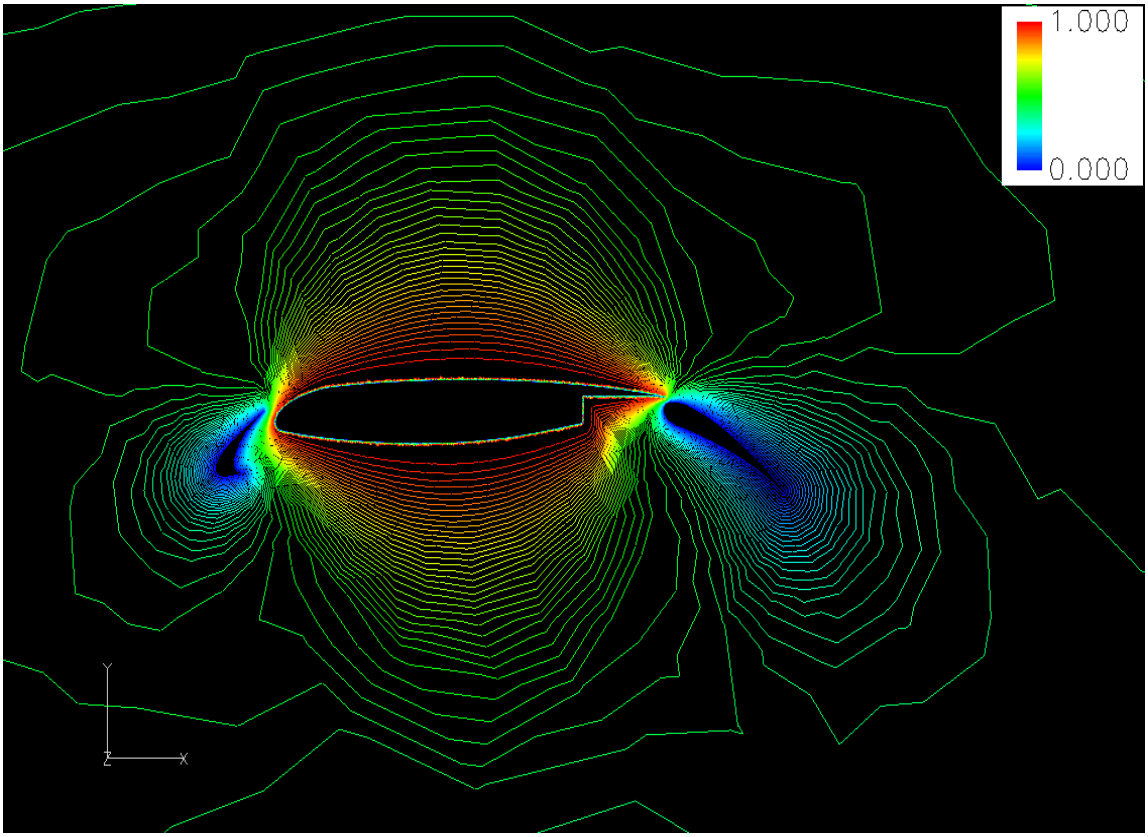

Figure 4.4: Weighting function of 3-element airfoil (main element)

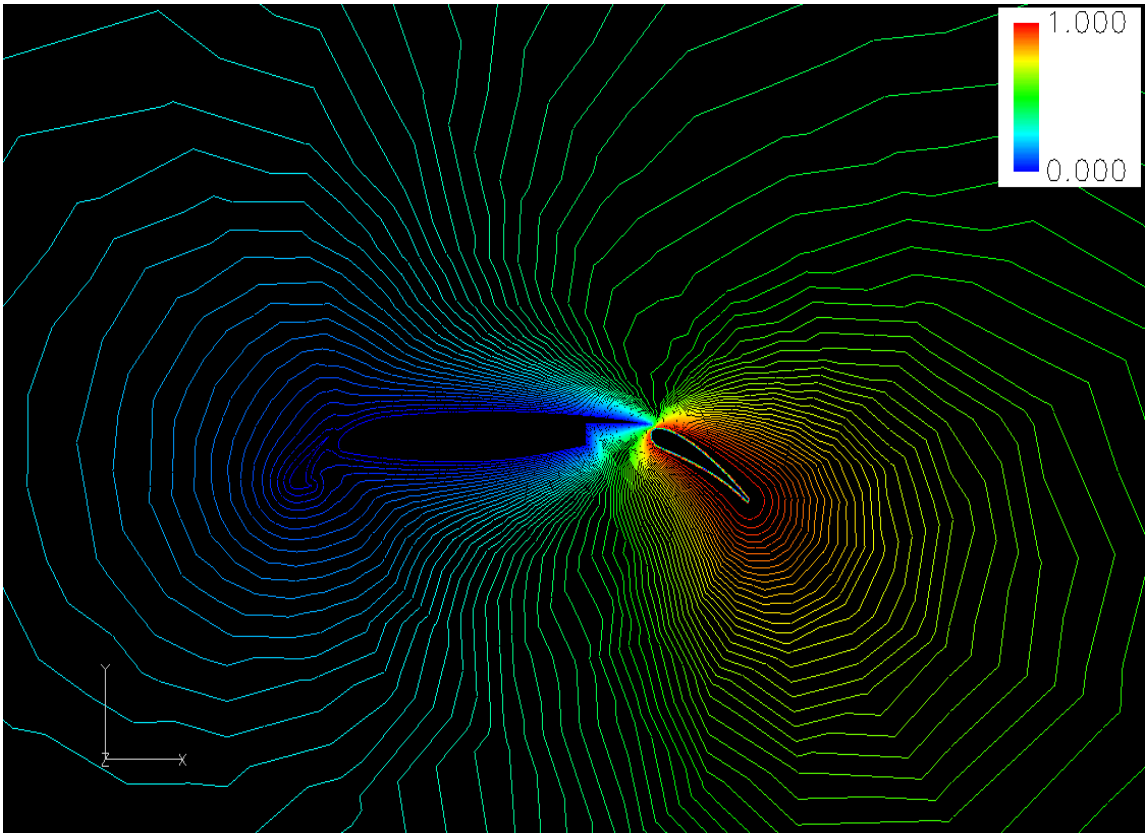

Figure 4.5: Weighting function of 3-element airfoil (flap)

Generally for point p, at least two connections are used for each surface (i.e., $nconnect = 2$) to avoid non-smooth variations in the distance function through the mesh. Increasing the number of connections can be considered as increasing the dissipation of the deformation scheme. As shown from Figure 4.6, *nconnect* does not have to be the same for every moving surface, which adds more flexibility and makes the scheme more efficient.

This method has several important properties. Most importantly, it requires no grid point connectivity information, and each point can be moved independently from its neighbors. This has two major implications: first, the scheme is universal and applicable to any grid type; unstructured, hybrid or structured with either single or multiblock data structures. Second, the scheme is perfectly suitable to a parallel platform and can be implemented efficiently since no communication is required between points or blocks. The motion of each point depends solely on its coordinate. Each data partition in a parallel environment can be updated independently from its neighbors so there is no connectivity data required, and the flow solver does not have to keep the grid motion parameterization data in its memory. The scheme accounts for moving surface rotations as well as translations, and this ensures grid quality is preserved by maintaining orthogonality even for large amplitude deformation. An important advantage with this approach is that the geometric quantities and weighting functions are only computed once at the beginning of the computation, so that during the deformation the grid can be updated quickly at each time step via equation (4.1) where only the moving surface parameters need to be processed.

4.2 Improved Algebraic Interpolation Method

In the original work by Allen (2006), the algebraic interpolation method is applied to a four-bladed lifting rotor in forward flight. For this purely rotating mesh movement case, grid quality is preserved by maintaining orthogonality very well. However, for cases involving

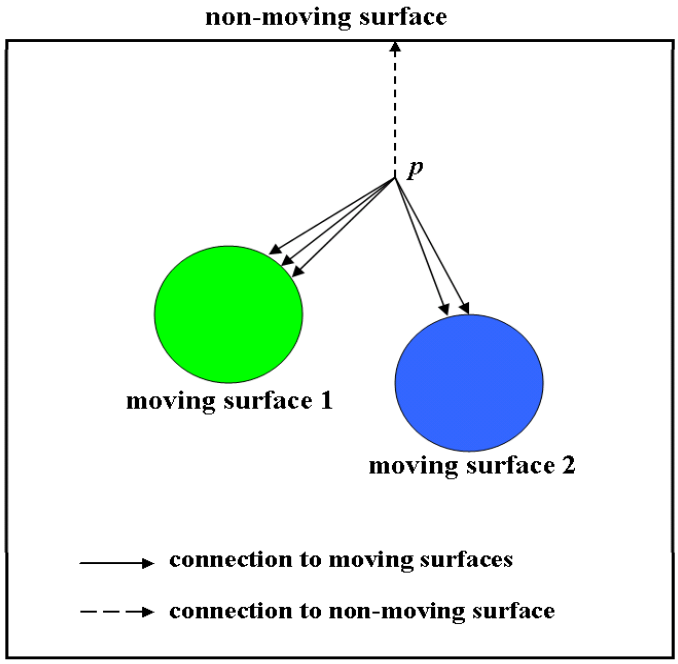

Figure 4.6: Connectivity diagram for field point

both rotation and translation, modifications to the original method must be performed to obtain acceptable mesh quality as described in this section. The constant parameter sr in equation (4.1) for calculating the rotation part of displacements is changed to an exponential function based on the relative distance function ψ

$$sr = 2^{6-\psi^{p,ns}} \tag{4.11}$$

This modification was found to be especially important for maintaining the grid quality in the viscous layer for the large amplitude two-node bending cases (see Figure 4.7). Additional resolution is added to the bow region above the top of the ship to resolve the air/water interface from water-on-deck events. Use of equation (4.11) was also required to eliminate negative volumes in this refined region. In general, when the deformed mesh from the original algorithm is lacking in overall grid quality, the application of mesh smoothing is used for improvement. A Laplacian based smoothing algorithm is implemented here,

since it is the most inexpensive way to perform mesh smoothing on structured/unstructured meshes by taking the average of neighboring nodes (Karman and Sahasrabudhe, 2007). For some test cases, the deformed mesh produced from the original scheme can end up with severe skewness and even negative control volumes due to a sudden transition of moving surface connectivity near concave surfaces and sharp corners (e.g., the stern profile of S175 container ship as shown in the middle of Figure 4.7). By smoothing the displacement vector $\Delta r^p = r^p(t) - r^p$ from equation (4.1), a new displacement vector $(\Delta r^p)'$ is obtained using the weighted average displacements of neighbor nodes as following:

$$(\Delta r^p)' = \left[\left(\sum_{nb=1}^{nnb} \frac{\Delta r^{p_{nb}}}{d_{p_{nb}}} \right) \left(\frac{nnb}{\sum_{nb=1}^{nnb} \frac{1}{d_{p_{nb}}}} \right) + \Delta r^p \right] \left(\frac{1}{nnb+1} \right) \tag{4.12}$$

where nnb is the number of neighbor nodes for p, $\Delta r^{p_{nb}}$ is the displacement vector of neighbor node p_{nb}, and $d_{p_{nb}}$ is the distance between node p and p_{nb}. As shown in Figure 4.7, the grid quality is improved significantly by adding the smoothing algorithm.

Additionally, extra neighboring connectivity is needed for points near concave surfaces to avoid negative control volumes during deformation. If the maximum *nconnect* which is equal to the number of neighbor nodes has been used and the mesh quality still needs to be improved, we will add extra connections copied from the field point's neighbor. This has been proven to help improve grid quality, especially for geometric profiles with concave surfaces.

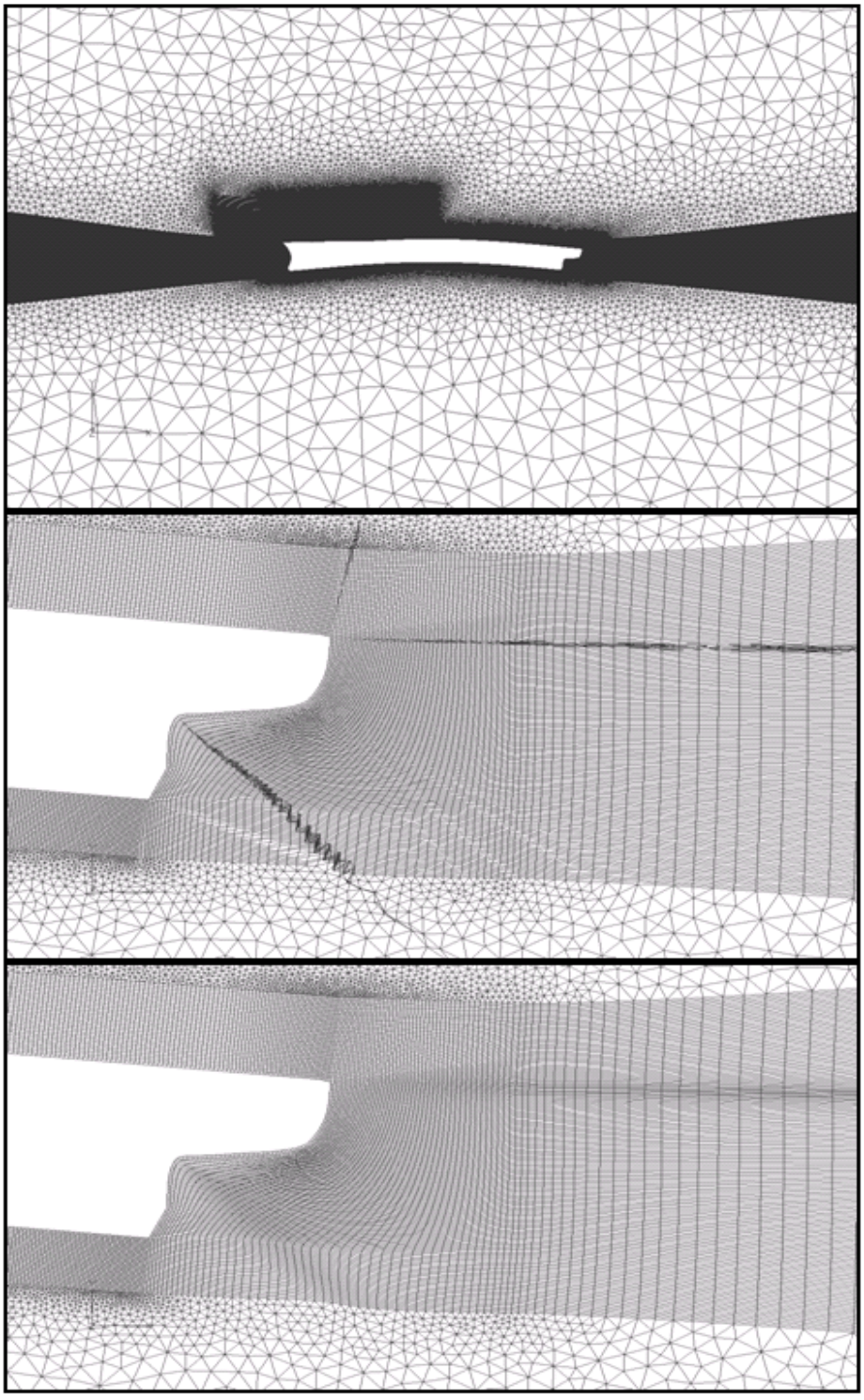

Figure 4.7: Two-node bending mesh deformation of S175 center plane (top): stern mesh details using original scheme (middle) in comparison with proposed smoothing improvement (bottom)

4.3 Parallelization

One of the most important features of the algebraic interpolation method is parallel efficiency. The scalability of the algebraic interpolation method on a parallel platform has been shown by Allen (2006), which is proven to be approximately $O(N^{2/3})$ (where N is the number of grid points). Also, this scheme scales linearly with number of moving surfaces, since the cost depends on computing the translation and rotation vectors of the moving surface points. During the process of implementing the algorithm into the SimCenter's in-house parallel unstructured flow solver *Tenasi*, some key parallelization issues are addressed in the following sections.

4.3.1 Building a Connection List for Each Field Point

As mentioned before, each field point can have a different number of connections. Since the calculation of distance and weighting functions are based on these connections, a connection list is needed for all the field points, which contains every connection node number as well as its subdomain number. For memory efficiency, only the information of the connection node that is closest to the field point needs to be saved in order to be memory efficient. If the data for other connection nodes are needed during computation, the node-surrounding-node map will be used to look them up.

4.3.2 Calculation of Distance and Weighting Functions

For each field point, the node to which it is connecting on the moving surface could belong to any domain. As shown in Figure 4.8, node 5 in subdomain-2 is connecting to node 1 on moving surface in subdomain-1. Thus, communication between the two domains is needed to assist the calculation of distance and weighting functions. The connection list described above, which serves as a map for each node, is vital during this process. First of all, the

identity information of field point (node 5) including its node number and coordinates is transferred to the paired domain (subdomain-1). Then on the domain where the connection node resides (node 1), some of the parameters for the distance and weighting functions are computed and passed back to the domain where the field point is stored (subdomain-2). Finally, the distance and weighting functions are calculated. For parallel efficiency, the information is transferred by batch, i.e., sending out data of each node all together from one subdomain to another.

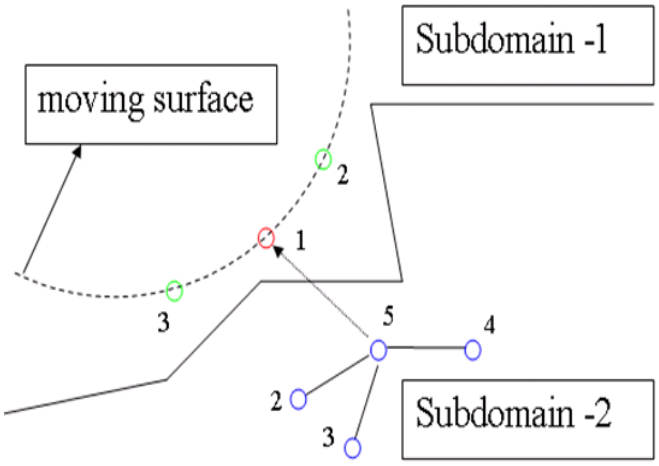

Figure 4.8: Schematic of parallel communication between subdomains.

Chapter 5

OVERSET GRID METHOD

5.1 Nomenclature

A brief description of a few terms in use in the overset community are as follows:

- Out Point: An out point is a solution node or cell that has been defined to be outside the domain of interest and should be excluded from advancement as a typical field point. The out points usually arise from overlapping grids with some portion of the grid inside a physical body or behind a symmetry plane.

- Fringe Point (Receptor Point): The points adjacent to the out points are fringe points and form a new boundary interior to the mesh and hence are also called inter-grid boundary points. Fringe points can also be found on outer boundaries of a mesh that is completely embedded in another mesh.

- Donor Point (Active Point): A donor is the interpolation source for providing the value to be applied at the fringe points. The donor will be composed of multiple donor members that provide the data from one or more locations in the donor grid or grids and will be multiplied by interpolation weights to produce the interpolated

value.

- Orphan Point: An orphan point is a fringe point for which no valid donor is available. The orphans can arise because of an error in marking of out points or because the grid system does not have sufficient overlap.

- Domain Connectivity Information: The domain connectivity information is composed of the specification of which nodes or cells are out, orphan, or fringe points along with the corresponding active point information specified by the donor members and the interpolation weights.

Overset grids for a 2D cylinder are shown in Figure 5.1 to help better understand each type of point mentioned above.

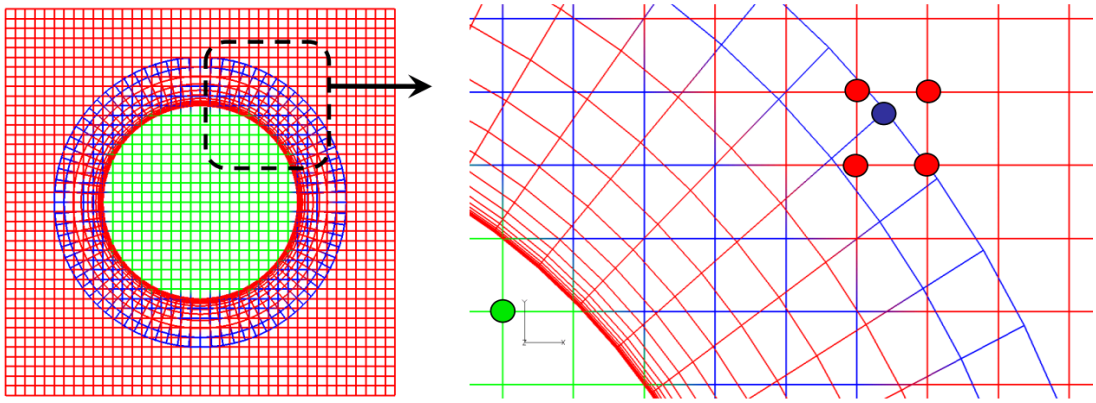

Figure 5.1: An example of overset grids, with donor points (red), fringe points (blue), and out points (green).

5.2 Implementation of Overset-Grid Capability

The approach for handling multiple moving bodies in relative motion problems in the present work is to construct a single composite grid from several overlapping grids using the SUGGAR grid assembly code (Noack, 2005b). SUGGAR is capable of handling structured, unstructured, and general polyhedral grids. It performs the hole cutting using an octree-based Cartesian approximation of the geometry with an XML file as input (XML is a text based language used to "mark up" data). It uses a standard neighbor walk search for locating the donors for a fringe point, with an initial guess for the donor search based on the octree. Overset-grid capability is implemented in *Tenasi* by leveraging a generalized library known as DiRTlib that encapsulates the basic overset functions related to the transfer of solution quantities across component grids. DiRTlib is a solver-neutral library that significantly expedites the addition of overset grid capability into existing flow solvers. It makes calls to a few solver-specific functions to interface DiRTlib with solver data in the computer memory. Two basic interface functions allow DiRTlib to obtain data from solver memory for use in donor interpolations and place data into solver memory for use at the fringe locations. DiRTlib also provides functions to read domain connectivity information and uses it to fill an "iblank" array given by solver with an integer flag that identifies fringe or out points to the flow solver. The flow solver uses this iblank information to modify the linear equation such that no updates to the solution are produced at the out and fringe points. Subsequently, the flow properties within the out points are set to an average of their neighboring node values. This treatment of the out points continuously updates the initial solution and therefore guards against an abrupt jump in the solution characteristics, should any of the out points become a field point after moving the body. Next, the flow solver makes a few strategic calls to the DiRTlib functions to transmit updated solution quantities from the donor points to the fringe points. The entire process is repeated at

each iteration/sub-iteration of the solution cycle. For the moving-body simulations, the flow solver uses additional DiRTlib functions to access the body transformations generated by SUGGAR and uses them to reposition the grid associated with a moving body.

Some challenges were encountered during the implementation of the overset capability into *Tenasi* flow solver. For example, DiRTlib will need to split the MPI communicator between the ranks on which the flow solver will execute and the rank on which SUGGAR will execute. The flow solver must also split the MPI communicator to obtain a communicator that is restricted to the flow ranks. The flow solver should use the split communicator instead of MPI_COMM_WORLD (the default communicator) so that the flow ranks may communicate with one another without involving the SUGGAR rank and collective operations of flow solver encompass only the flow ranks.

The current overset-grid framework has been developed in *Tenasi* for both static and dynamic simulation capability. For the dynamic cases presented in this work, motions of the moving bodies are prescribed by user-defined functions, although full 6DOF simulations may also be performed within the *Tenasi* framework. Figure 5.2 outlines the procedure employed for the dynamic case simulations. Because of the overlapping nature of the grids, the "solve flow equation" segment shown in the flowchart needs some extra work on solution update than on a single grid. Solutions with fringe point BCs are frozen during the current iteration step, and then are updated in the next iteration.

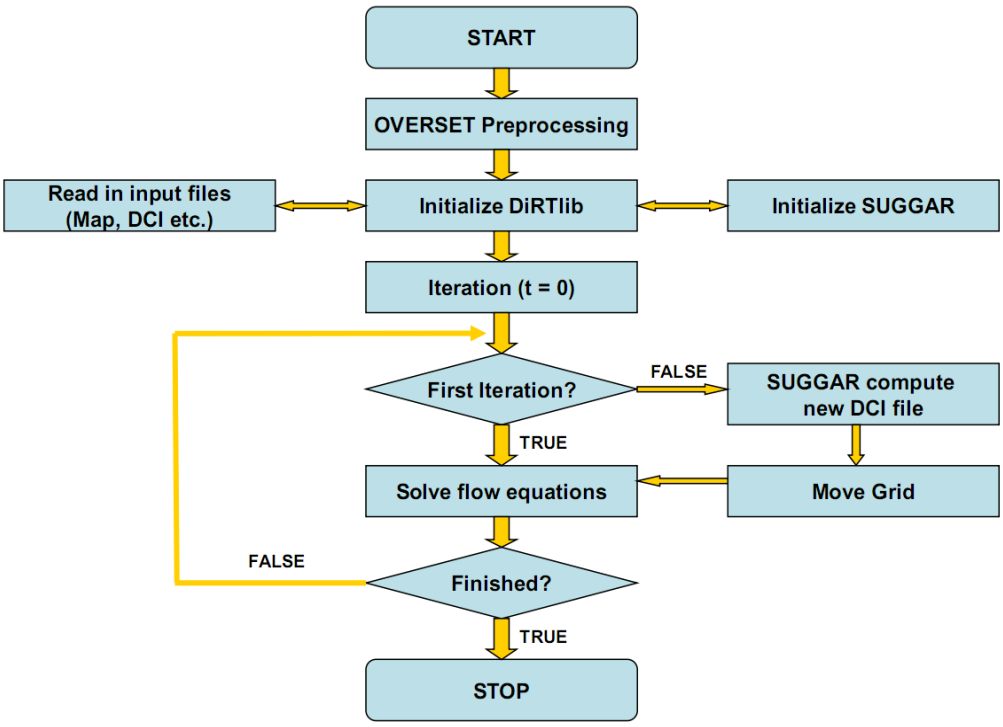

Figure 5.2: Flowchart of overset methods coupling with flow solver for dynamic case simulations

Chapter 6

RESULTS AND DISCUSSION

6.1 AIM Test Cases

Initially, the improved AIM approach was tested by rotating a NACA0012 airfoil 90 degrees counterclockwise while keeping the far field boundary fixed. As shown in Figure 6.1, the deformed mesh with viscous wall spacing has very good quality and the grid structure around the airfoil is preserved very well even for such large angle rotation. Not surprisingly, the original algorithm was able to successfully perform this deformation. Next, the 2D NACA0012 airfoil and 3D Suboff geometries were deformed vertically $\Delta y(x,t)$ along the longitudinal x-axis using harmonic two-node bending

$$\Delta y(x,t) = A \sin\left[\frac{x - x_0}{x_L - x_0}\pi\right] \sin\frac{2\pi t}{\tau} \tag{6.1}$$

where x_0 and x_L denote the axial positions of the two nodes of zero displacement. For this test case, $x_0 = 0$ and $x_L = 1$. An amplitude $A = 0.05$ and period $\tau = 1$ were used. The mesh from the original AIM approach showed unacceptable quality and negative volumes in regions with connections to concave surfaces, similar to those detailed in Figure 4.7. With improvements to the AIM approach described in the previous section, both the 2D

and 3D test cases show good quality as shown in Figure 6.2. Unsteady flow simulations for the NACA and Suboff geometries undergoing two-node bending in still fluid were also successfully performed to verify the mesh quality.

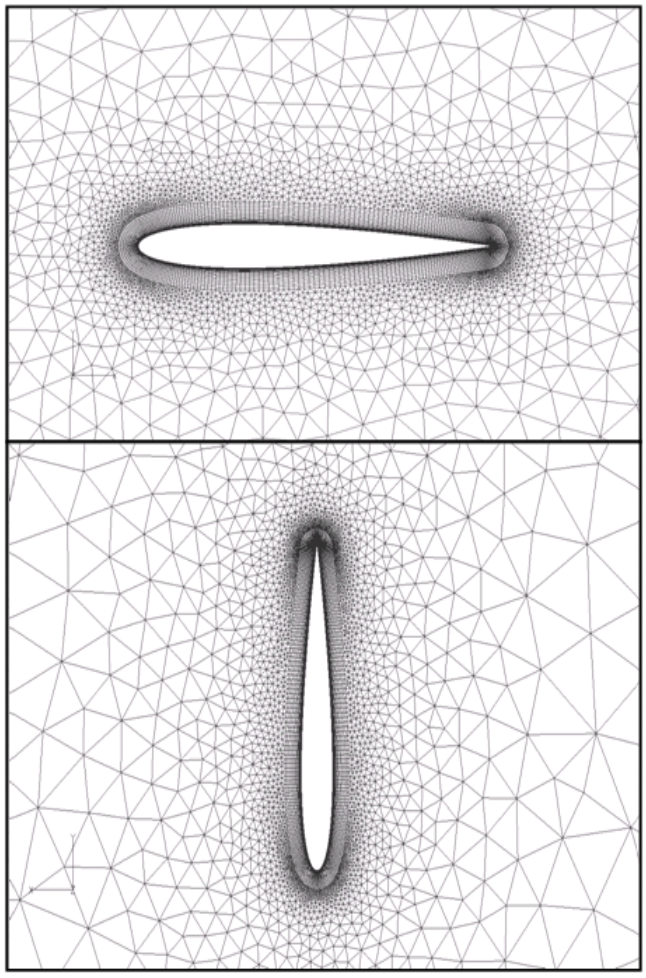

Figure 6.1: 2D NACA0012 airfoil at original position (top) and after 90 degree counter-clockwise rotation (bottom).

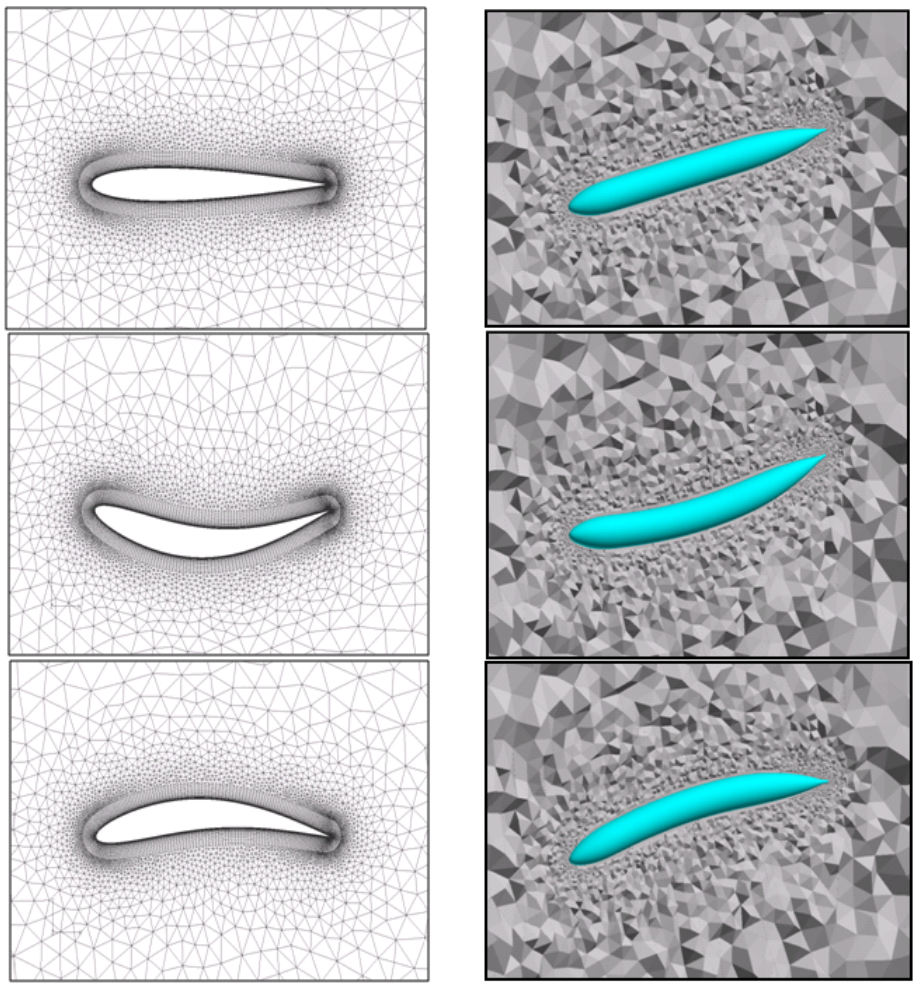

Figure 6.2: 2D NACA0012 airfoil (left) and 3D Suboff (right) from undeformed (top) to sagging (middle) and hogging (bottom) deformation respectively.

6.2 Verification of Synthetic Jet Cases

The synthetic jet test cases from the well known NASA Langley Research Center workshop - "CFD validation of synthetic jets and turbulent separation control" at Williamsburg, VA in 2004 (Rumsey *et al.*, 2004; Yao *et al.*, 2006), have been used for further test and verifications. Experiments were performed at NASA Langley Research Center using multiple instrumentation systems including particle image velocimetry (PIV), laser doppler velocimetry (LDV) and hotwire probes. All three cases include a vibrating membrane/diaphragm in the configuration, which is similar to two-node bending in some fluid-structure interaction applications. With increasing geometric/physical complexity, they are designed for CFD validation.

Most researchers used approximate methods in implementing the moving diaphragm, such as using periodic velocity at inlet/outlet (the so called nonmoving-wall transpiration boundary condition) or adopting Cartesian grid plus immersed boundary conditions (Cui and Agarwal, 2004). As the only participants using moving grid boundary condition, Xia and Qin (2005) suggested that the direct simulation of the diaphragm oscillation is the most straightforward and accurate method for the study of the flow in the plenum chamber, which in turn can have a significant effect on the synthetic jet flow. They proposed a dynamic grid methodology based on a spring analogy model to treat the oscillating diaphragm in Case 1 and Case 2. No direct simulation of the diaphragm vibration for Case 3 has been found in published literature at this point. As summarized by Rumsey (2008), whether a predictive BC (moving wall) should be used to achieve close agreement with velocities at the orifice is one of the remaining challenges so far. In this work, the algebraic interpolation method was used to directly simulate the movement of the diaphragm. As mentioned earlier, AIM is much less expensive compared to the spring analogy based methods. Below, some preliminary CFD validation for Case 1 is presented, as well as mesh deformation for Case 2

and 3. The flow field solution for both Case 2 and Case 3 will be included in future work.

In Case 1 (synthetic jet into quiescent air), an isolated synthetic jet (1.27mm wide) exhausting into ambient quiescent air is formed by a single diaphragm driven by a piezo-electric actuator. The diaphragm which is approximately 50mm (1.98 inches) in diameter is deformed in a trapezoidal-shaped drum-like fashion. A 2D structured grid is built for the test as shown in Figure 6.3 and 6.4 respectively. During the deformation, the maximum oscillating amplitude of the diaphragm is 4% of its diameter, or about 2mm. A converged steady state solution without grid motion is first obtained, after which the diaphragm starts to oscillate. Here, as many researchers have investigated in the workshop, computational results with experimental data near the slot exit are compared. The one equation Menter SAS model was used in the simulations. As shown in the Figure 6.5, the solution of v-velocity at $y = 0.1$mm above the synthetic jet exit is in reasonable agreement with the PIV and Hotwire data, which justifies that the boundary movement employed at the diaphragm in our simulations is applicable to resemble the experimental set-up and that the deformed meshes are of good quality.

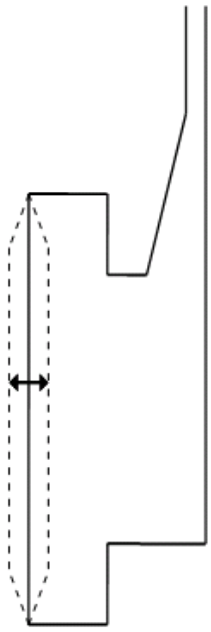

Figure 6.3: Schematic of oscillating diaphragm movement of the synthetic jet in Case 1.

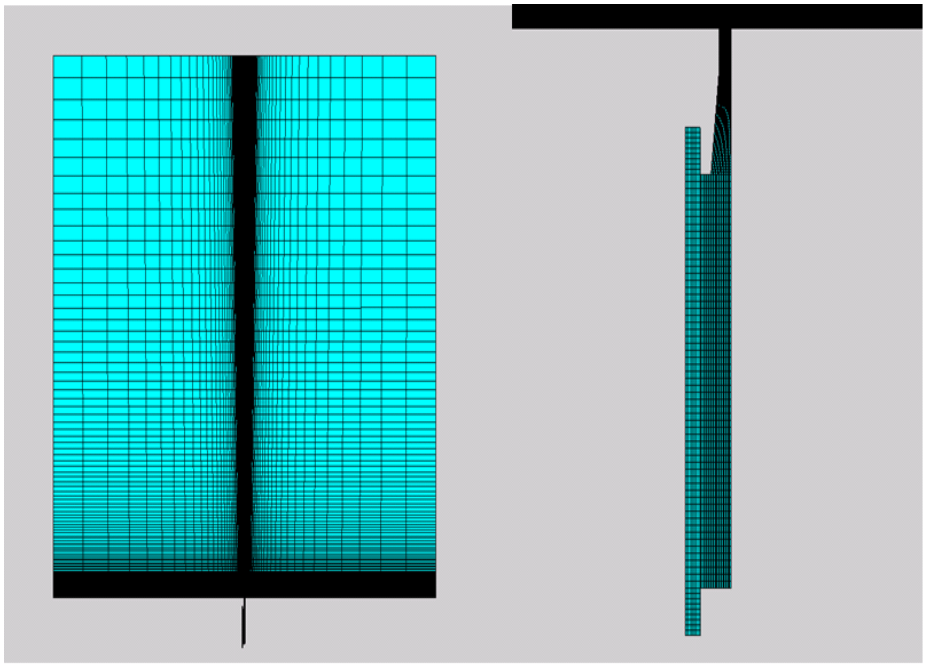

Figure 6.4: Mesh generated for Case 1 in full view (left) and the close-up of synthetic jet (right).

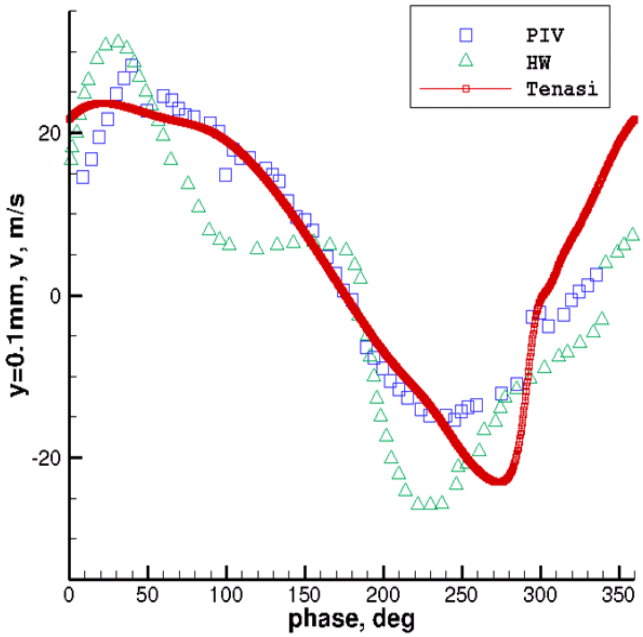

Figure 6.5: V-velocity near the slot exit of synthetic jet.

A quarter phase sequence of velocity vectors and vorticity contours for the synthetic jet into quiescent fluid is shown in Figure 6.6. The phases correspond to the undeformed, minimum volume, undeformed, and maximum volume diaphragm configurations. The figure shows the generation of a jet issuing into the still fluid and associated vorticity during the undeformed to minimum volume phase of the oscillating diaphragm. As the diaphragm expands to its maximum volume, the jet reverses and fluid is entrained into the diaphragm. An additional simulation was performed with the synthetic jet issuing into a boundary layer in cross flow from left to right. Results in Figure 6.7 show the impact of the synthetic jet on the boundary layer and on convection of the vorticity by the cross flow.

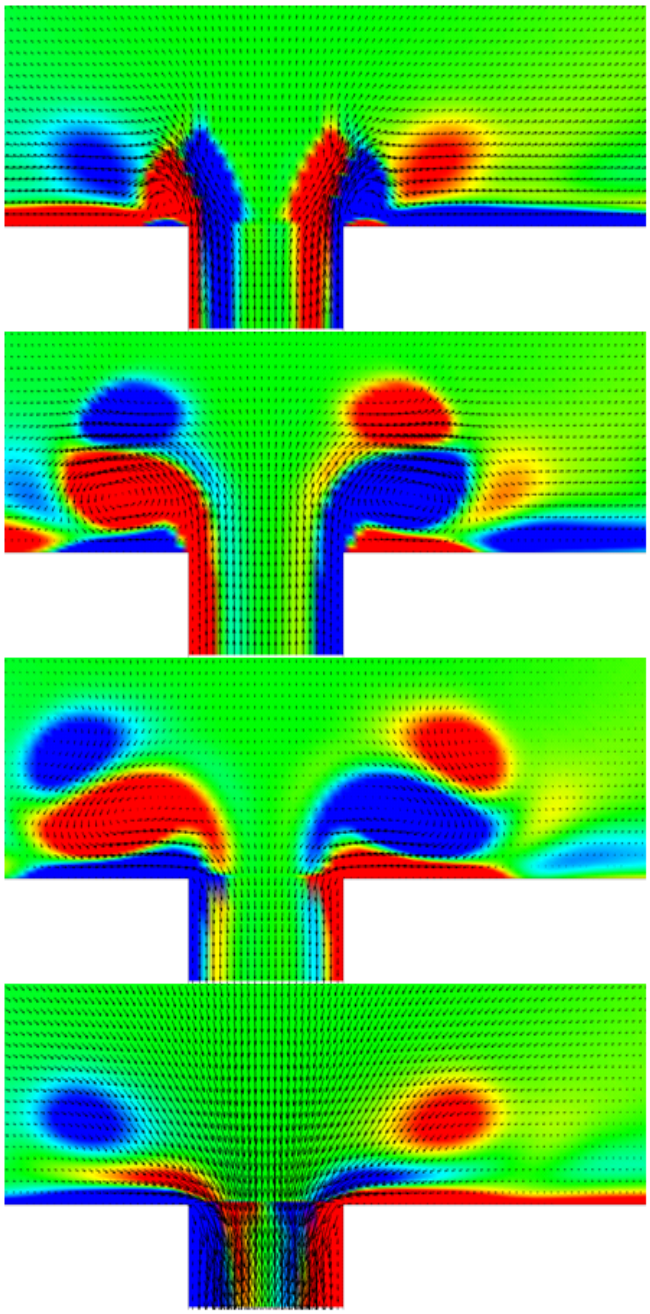

Figure 6.6: Quarter phase velocity vectors and vorticity contours for synthetic jet into quiescent fluid. Phases from top to bottom correspond to undeformed, minimum volume, undeformed, and maximum volume diaphragm configurations.

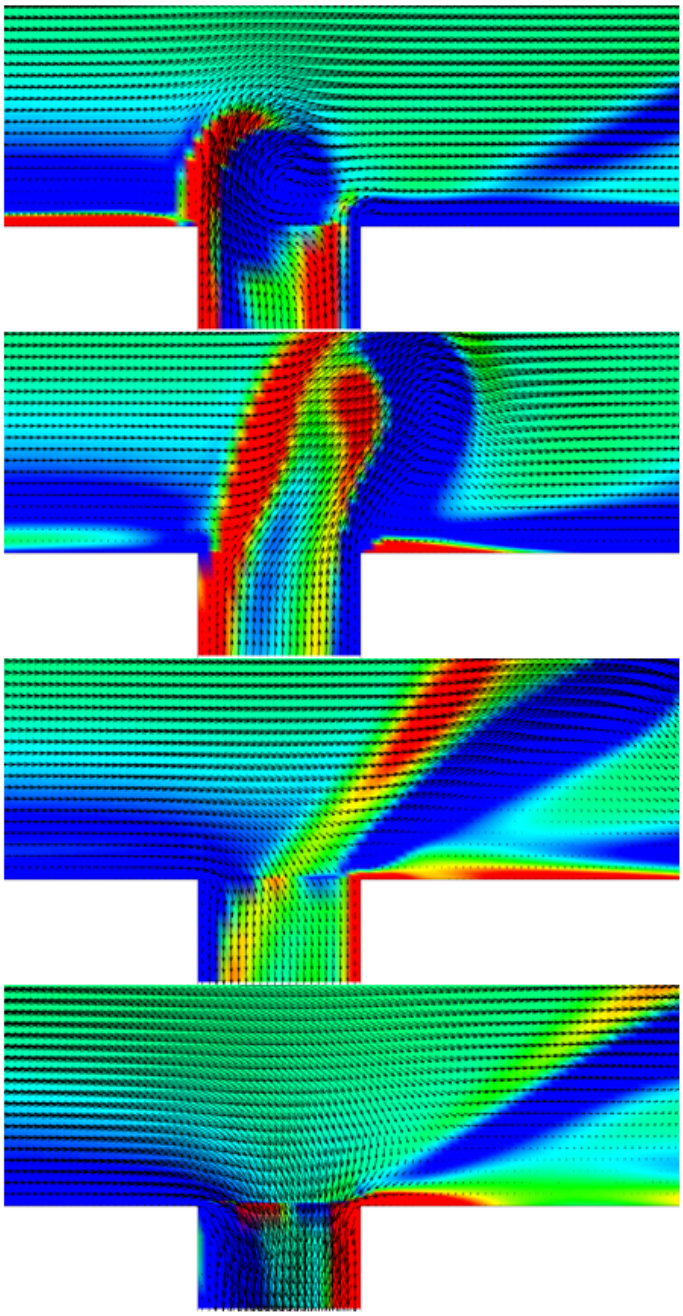

Figure 6.7: Quarter phase velocity vectors and vorticity for Case 1 synthetic jet into cross flow boundary layer.

In Case 2 (synthetic jet into a crossflow), flow is passed in and out of a circular orifice (6.35 mm in diameter), which was located on the floor of a wind tunnel splitter plate with a turbulent boundary layer at $Mach = 0.1$ and approximate boundary layer thickness of 21 mm. The jet is driven electro-mechanically by a square-shaped rigid piston mounted on an elastic membrane inside the cavity chamber beneath the splitter plate. The cavity under the orifice is extremely shallow (1.77 mm deep) and the piston moves up and down from a neutral position. A schematic of the configuration of cavity chamber is shown in Figure 6.8. A 2D unstructured grid is built for testing the mesh deformation induced from the motion of vibrating membrane. Due to the symmetric structure, only the left half of the deformed meshes are shown in Figure 6.9, concentrating on the cavity chamber. The produced meshes show good quality with the membrane deformed up and down at maximum amplitude. However, the flow field solution is needed for further validation, as Rumsey *et al.* (2004) concluded that among all the participants of the aforementioned workshop, no one method, algorithm or turbulence model stood out as being the best methodology. The investigation of this case will be continued and other researchers' progress will also be followed.

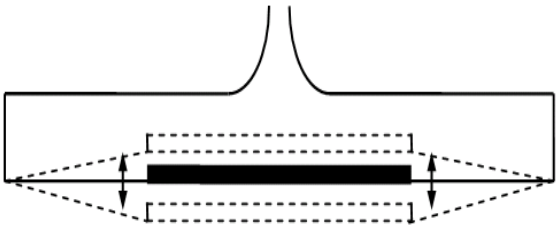

Figure 6.8: Schematic of oscillating diaphragm movement of the synthetic jet in Case 2.

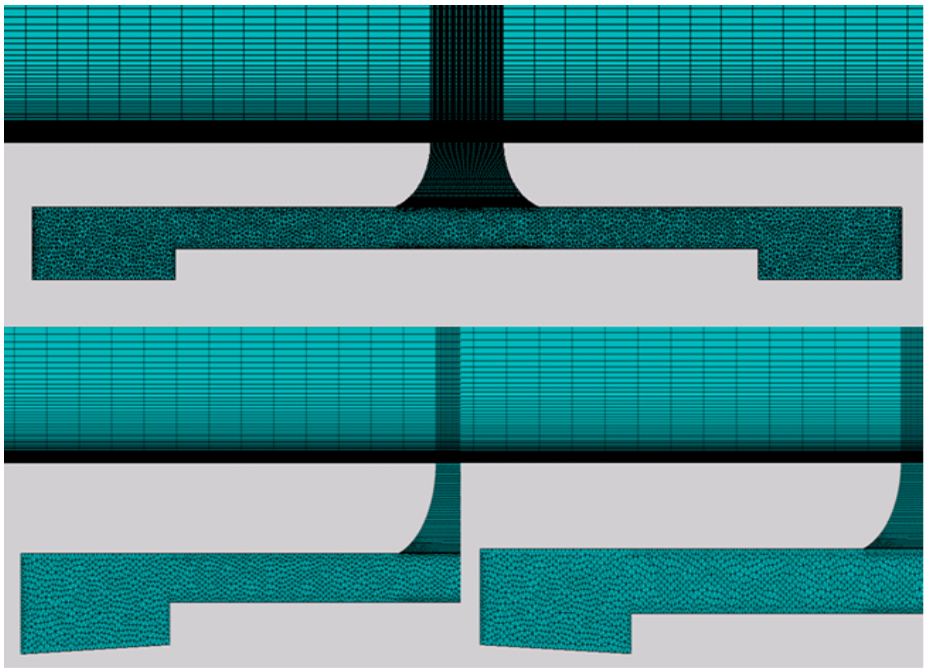

Figure 6.9: Mesh deformation in Case 2: undeformed mesh (top), with piston moving up (bottom left), and down (bottom right).

In Case 3 (turbulent flow over a hump model), a separated flow over a wall-mounted two-dimensional hump was controlled by a zero mass-flux oscillatory jet or suction through a slot as shown in Figure 6.10. Unlike the previous two cases, no published literature has been found studying the moving grid BC for this case. So here some preliminary work with respect to purely mesh deformation has been done without flow field solving. A 2D structured grid is built for this case. And the deformed meshes are shown in Figure 6.11. The overall grid structure is preserved very well even with large amplitude movement of the membrane (the maximum amplitude is about 20% of the length of membrane).

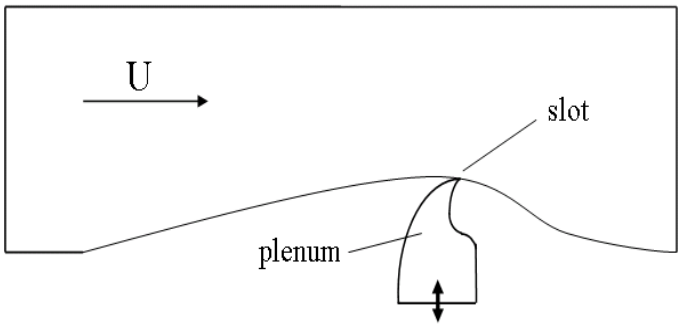

Figure 6.10: Schematic of flow over a hump in Case 3.

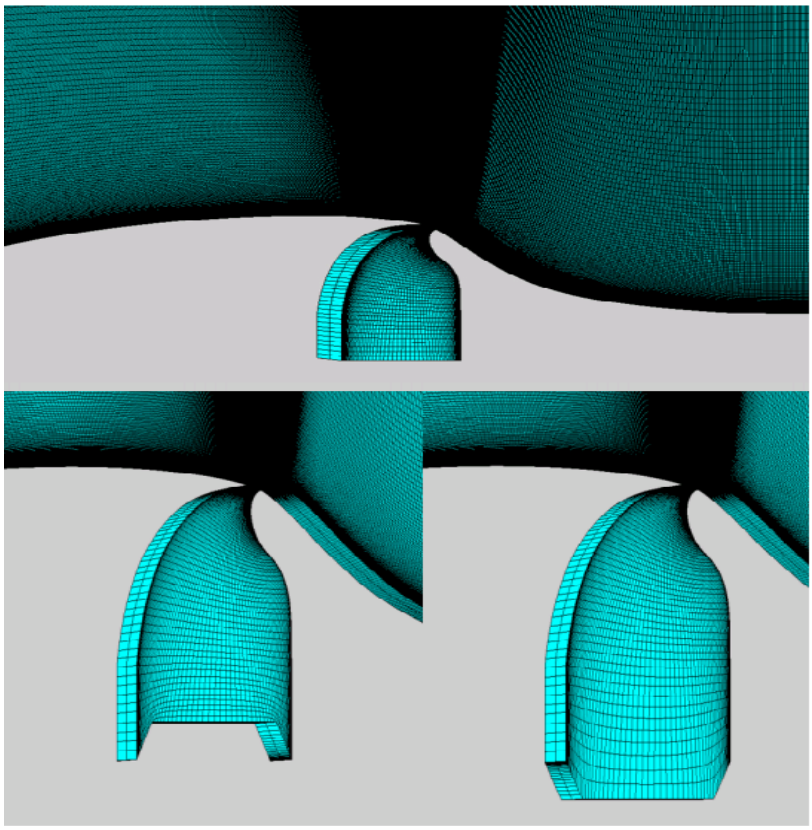

Figure 6.11: Mesh deformation in Case 3: undeformed mesh (top), with the piston moving up (bottom left), and down (bottom right).

6.3 FSI Application for S175 Container Ship

One of the prime motivations for adopting this mesh deformation scheme is to apply it to ship hydrodynamic applications. The final goal of this research is to perform fully coupled fluid-structure interaction for the S175 container ship, where the hull and volume grids are deformed at each time step in response to hydrodynamic loads. Wilson *et al.* (2006a; 2008) studied ship hydroelasticity using a one-way coupling where the unsteady hull forces from the RANS solution were used to perform a structural wet-mode analysis. The unsteady RANS simulations with rigid body pitch and heave motions in both moderate and large amplitude incident waves showed good agreement with experimental data from Ramos *et al.* (2000).

The SimCenter's in-house parallel unstructured flow solver, *Tenasi*, was used in this simulation. The turbulence models available in *Tenasi* include: the one equation Spalart-Allmaras model, the one equation Menter SAS model, the two-equation q-omega model and the two-equation k-omega/k-epsilon hybrid model. The one equation Menter SAS model was used in the simulations. The Tenasi solver's ability to predict large amplitude motions of the S175 container ship in incident waves has been demonstrated by Wilson *et al.* (2008).

For the fluid-structure interaction application with S175 container ship, the unstructured grid contains 337,878 nodes and is decomposed into 8 blocks. The simulations were performed on 8 processors of SimCenter's in-house DELL PowerEdge 1950 parallel cluster. A steady flow solution with regular incident waves at $Fr = 2.0$ and $Re = 1.0e6$ was obtained first while the ship was fixed without motion and no mesh deformation was applied. Then unsteady simulations were performed until the solution started to show periodic behavior. At each time step of the unsteady run, the hull geometry profile was deformed by a user-defined function in a drum-like fashion. Three Newton's iterations were used for every time step. It took about 4 wall clock hours to complete a period of deformation. As shown from

Figure 6.12, the resulting deformed meshes have shown good quality and enable the flow solver to capture the "roll-up" and shedding of the air-water interface from bow to stern along the ship surface.

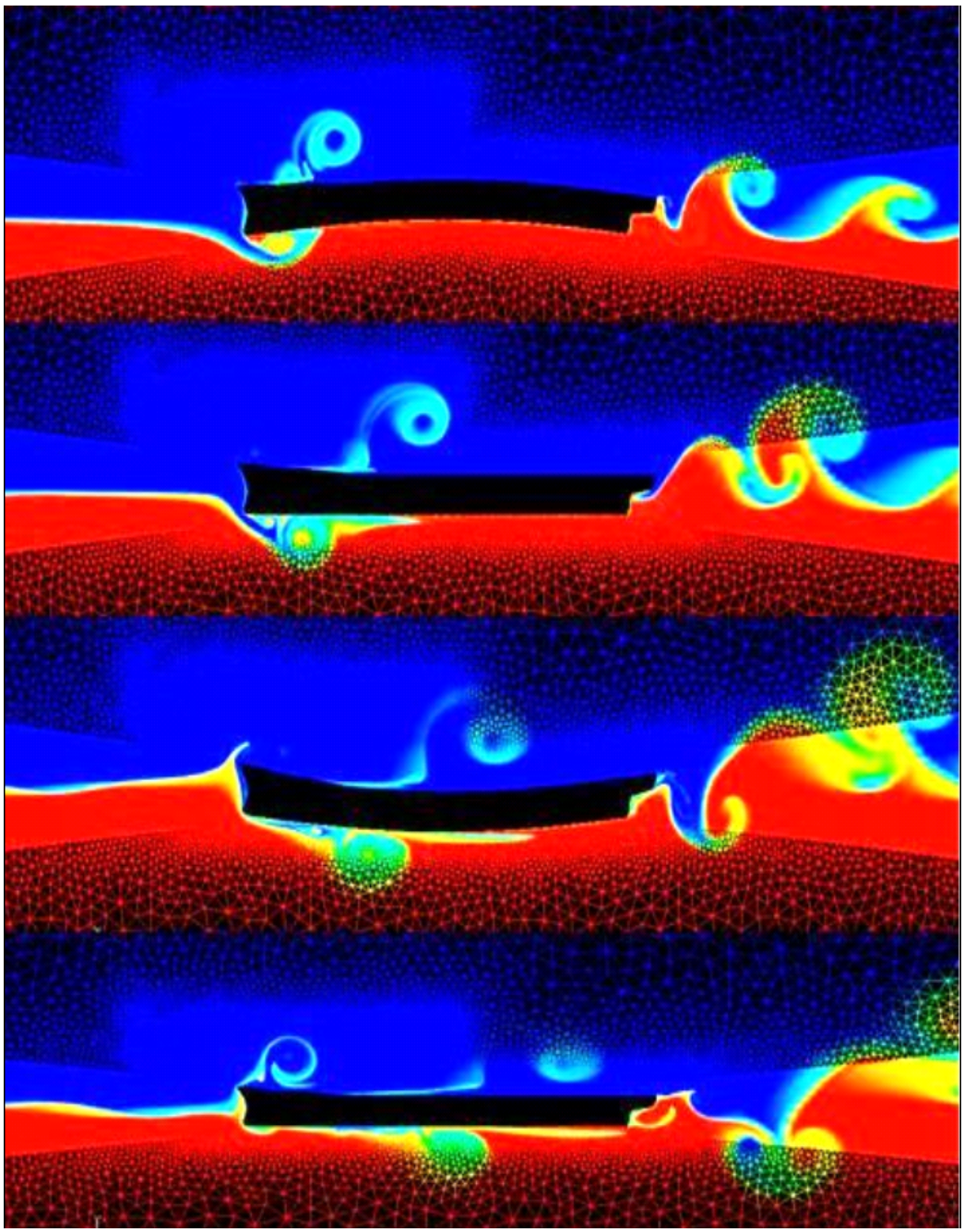

Figure 6.12: Quarter phase sequence for S175 container ship center plane geometry during harmonic two-node bending. Contours indicate free surface evolution of air (blue) and water (red).

6.4 Overset Grids Method Test Cases

6.4.1 Static Cases

First, incompressible flow past a 2D static cylinder was tested. The overset grids consist of an O-type grid (cylinder) and a structured grid (background). Both grids were created in an extruded-2D-grid fashion from mesh generation software *Pointwise*. Grid tools developed at SimCenter were used to concatenate these two grids together into overset grids, which has 10083 nodes in total. Steady viscous flow solutions were obtained using q-omega two-equation turbulence model at $Re = 1e5$. Pressure contour, x-velocity contour, and velocity vectors are shown in Figure 6.13, Figure 6.14, and Figure 6.15 respectively. Second, incompressible flow past a sphere was tested. Similar to the construction of the cylinder case, the overset grids consist of an O-type grid as sphere and a structured grid as background, with about 3.4 million nodes in total. Steady viscous flow solutions were also obtained using q-omega two-equation turbulence model at $Re = 1e5$. Results are shown in Figure 6.16 and Figure 6.17.

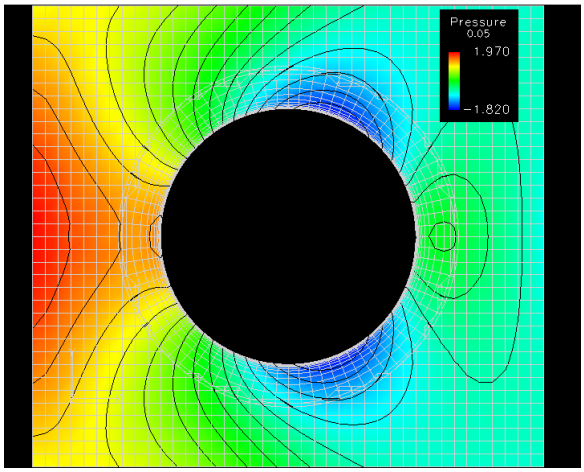

Figure 6.13: Pressure contour of flow passing a 2D cylinder.

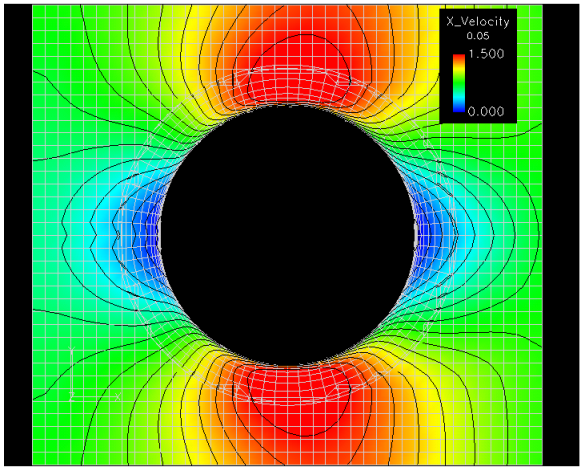

Figure 6.14: X-Velocity contour of flow passing a 2D cylinder.

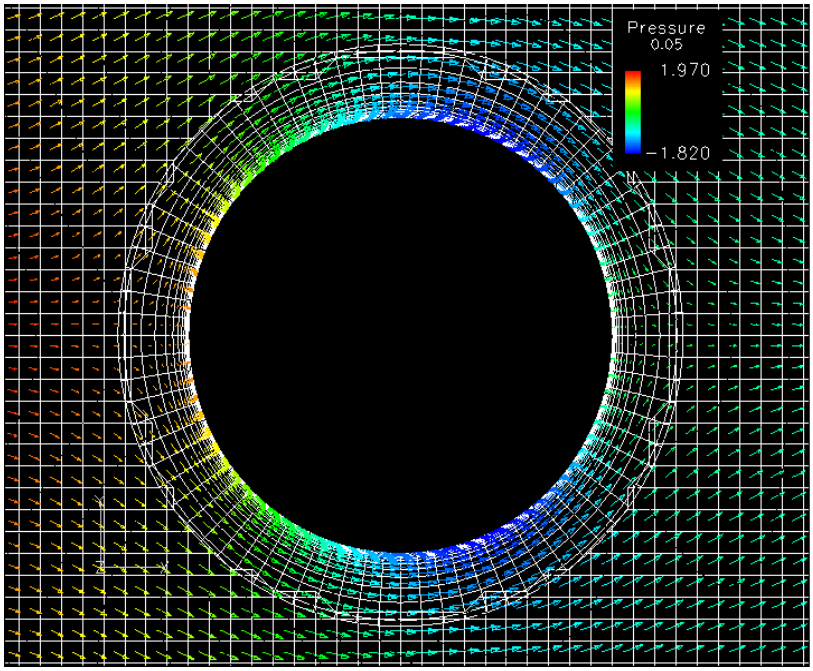

Figure 6.15: Velocity vectors of flow passing a 2D cylinder.

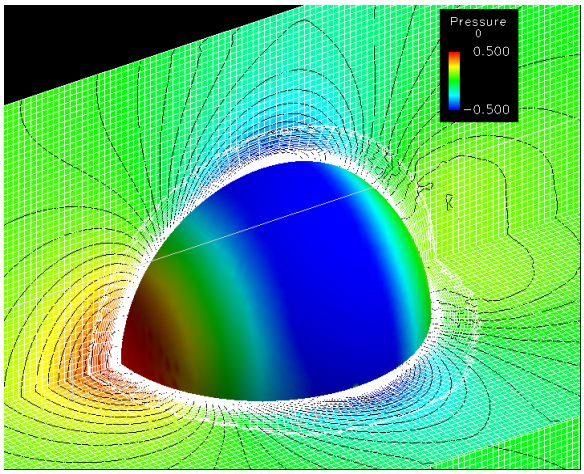

Figure 6.16: Pressure contour of flow passing a sphere.

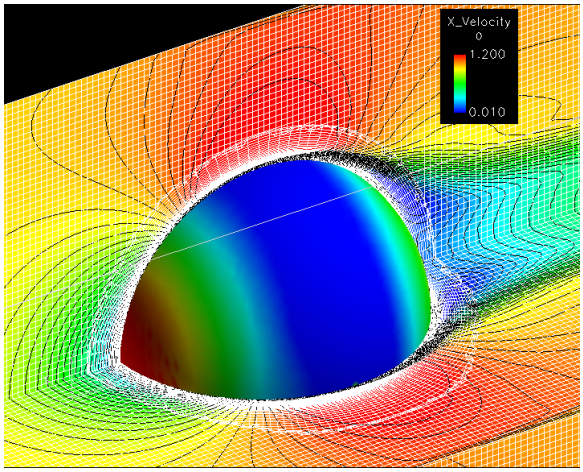

Figure 6.17: X-Velocity contour of flow passing a sphere.

6.4.2 Dynamic Cases

A few test cases were studied first, including single oscillating cylinder and two oscillating cylinder interaction, in order to prepare the foundation for investigation of ship-Suboff interaction.

6.4.2.1 An Oscillating Cylinder Test Case with Verification

The overset grid method's capability for handling moving bodies simulation was first tested on an oscillating cylinder. The overset grids are the same as the one used in the static case. The motion of the oscillating cylinder is prescribed by $x = A\sin(\omega t)$, with an amplitude of a quarter of radius of the cylinder ($A = 0.25$) and frequency of $\omega = 4.0$. 400 time steps was used per period. Unsteady viscous flow solutions were obtained using q-omega two-equation turbulence model at $Re = 1e5$. Results are shown in Figure 6.18 and Figure 6.19.

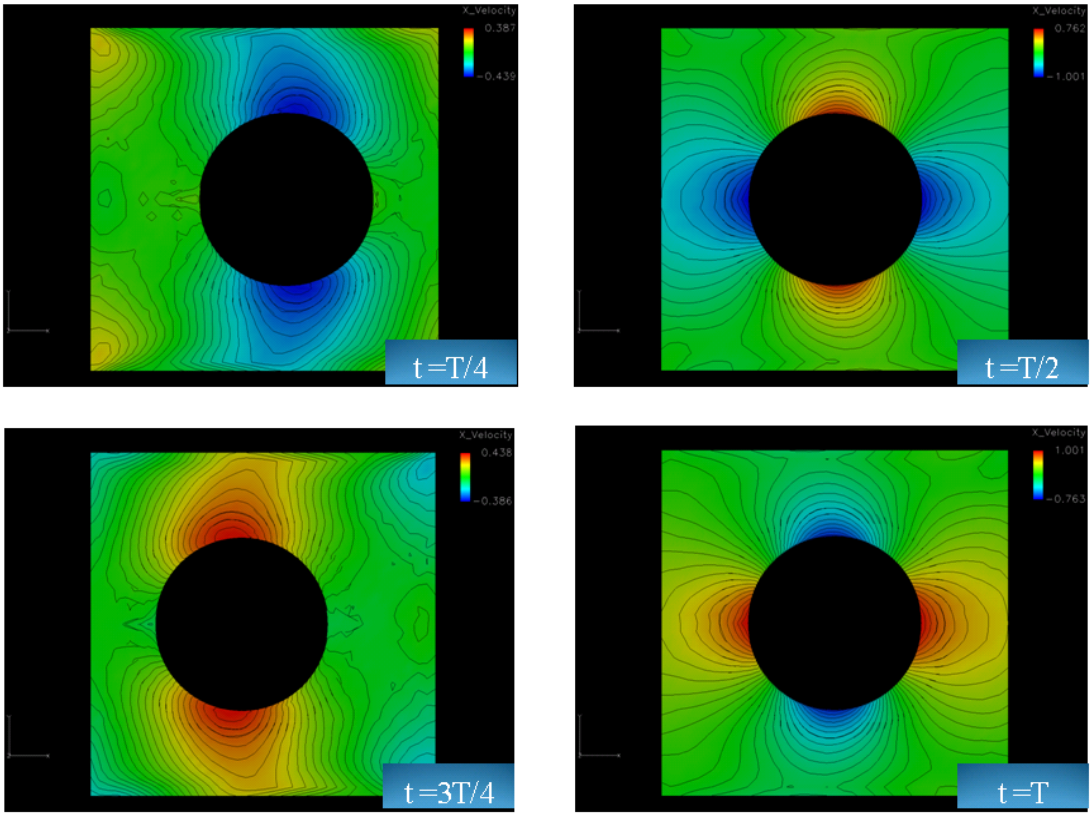

Figure 6.18: X-Velocity contours of an oscillating cylinder in one period.

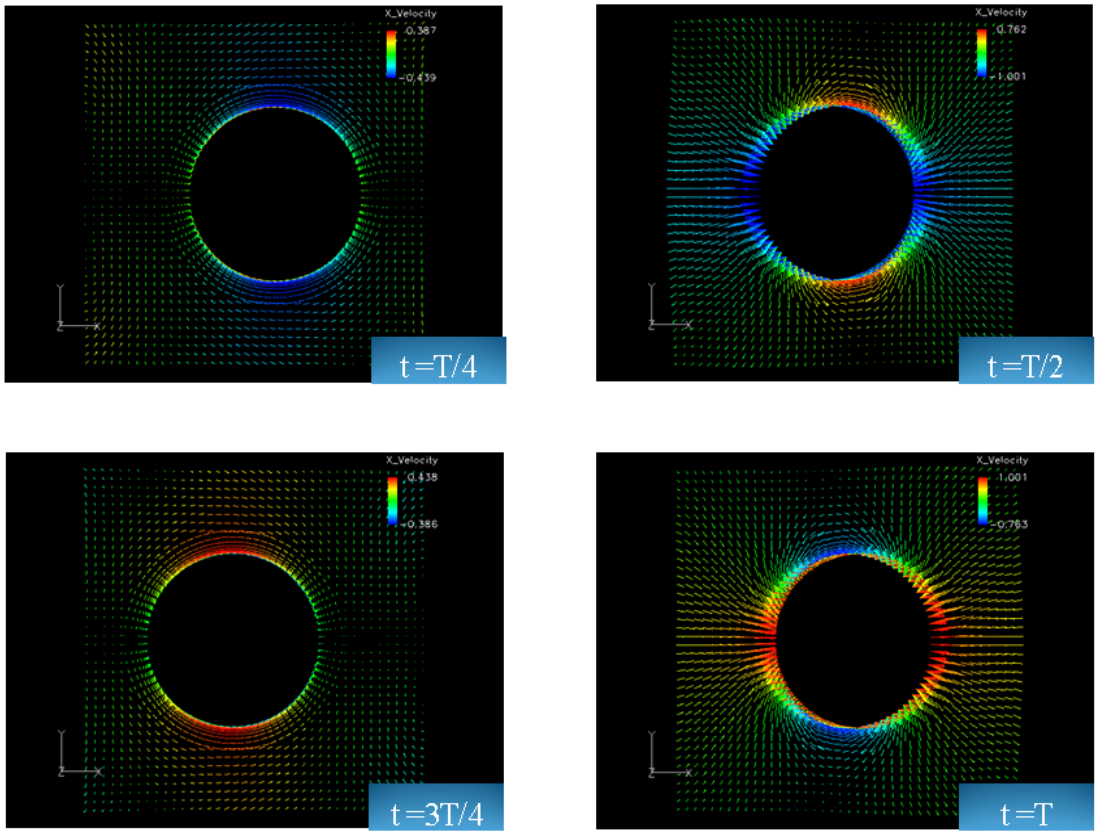

Figure 6.19: Velocity vectors of an oscillating cylinder in one period.

A baseline configuration was set up to verify the solution obtained from overset grids method. A single grid with the same inner grids as overset case was made, as shown in the Figure 6.20. The entire grid was prescribed for movement with the same function as the overset-grid configuration, $x = A\sin(\omega t)$ (i.e., no relative motion between the cylinder and the farfield boundary). Using the same flow parameters, solutions were obtained and compared with the ones from the overset-grid configuration at the same number of time steps (i.e., $t = nT$, where T is the period, and $n = 1, 2, 3, ...$), as shown in Figure 6.21 and Figure 6.22. Both pressure contours and x-velocity contours between two configurations agree well, especially in the near-cylinder region, which can be explained by the fact that grid resolutions are matched very well in that area. On the other hand, more noticeable differences from the farfield are mostly due to the increasing grid resolution disparity. Overall, sufficient solution accuracy is provided by the overset grids method with the ease of generating simple structured grids, and its advantages are further demonstrated in the following applications.

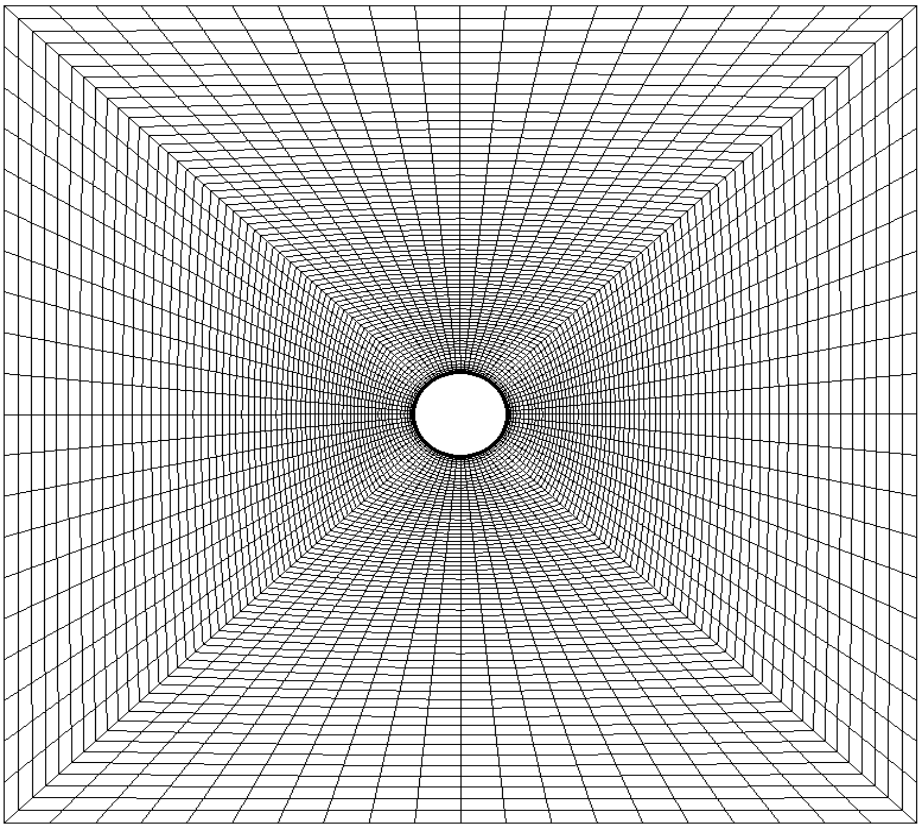

Figure 6.20: Single grid for the basline configuration.

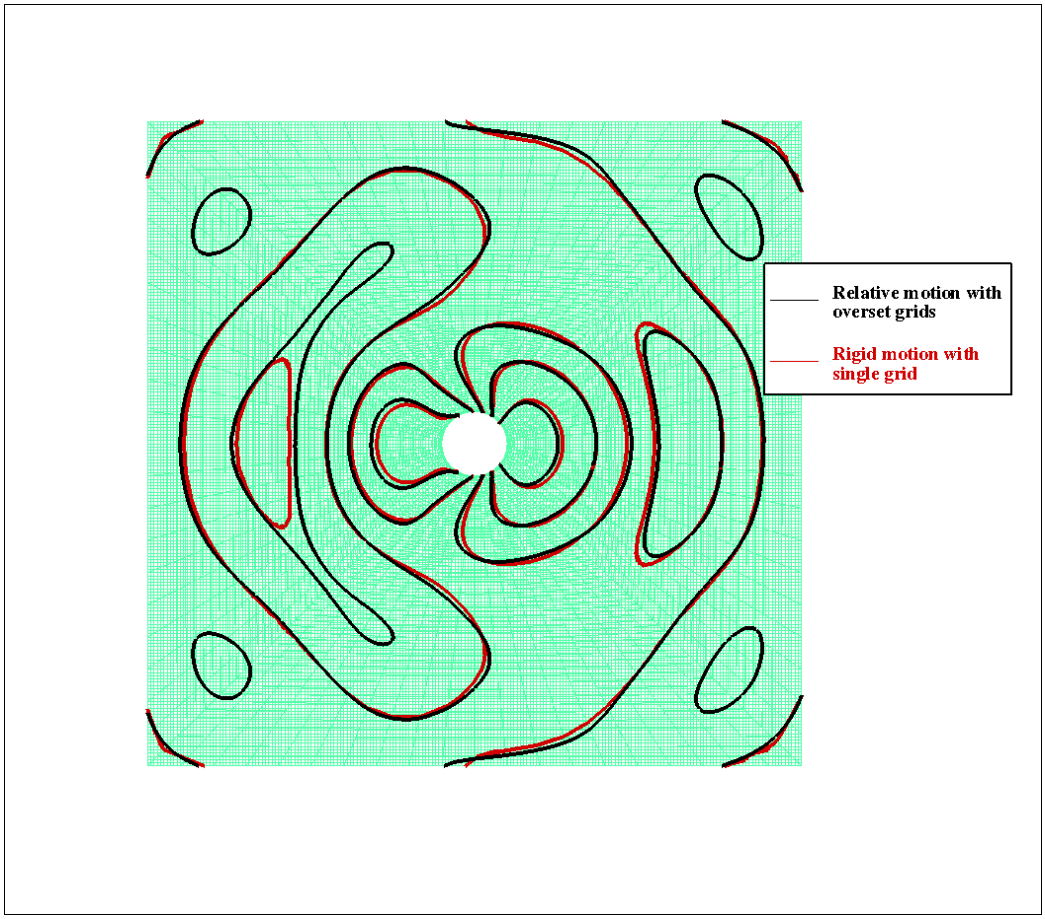

Figure 6.21: Comparison of pressure contour between the baseline configuration and overset-grid configuration.

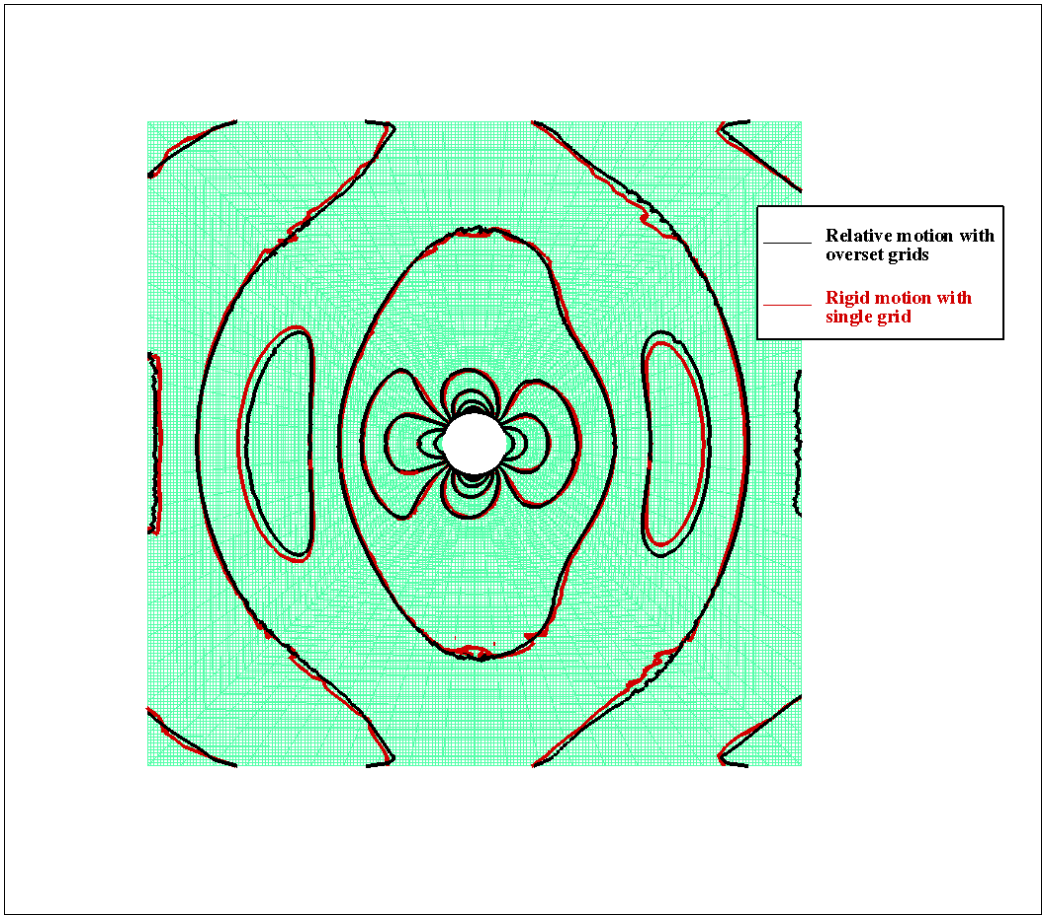

Figure 6.22: Comparison of X-Velocity contour between the baseline configuration and overset-grid configuration.

6.4.2.2 Two Oscillating Cylinders Interaction

The ability of overset grid method for handling multiple bodies in relative motion was firstly tested on two oscillating cylinders which are prescribed with same amplitude and frequency but 180-degree phase difference by $x = A\sin(\omega t)$. In this case, $A = 1.0$ and $\omega = 1.0$. Two cylinders are separated by a quarter of the cylinder diameter. As before, 400 time steps was used per period. Local mesh refinement was needed in the middle of the background grid to provide sufficient overlap with the cylinder grids and thus eliminating orphan points, especially when the gap between two cylinders is small and the cylinder grids are also overlapping. Unsteady viscous flow solutions were obtained also using q-omega two-equation turbulence model at $Re = 1e5$. Results are shown in Figure 6.23 and Figure 6.24. From the pressure contours, significant low-pressure region can be identified when cylinders are passing each other (i.e., at $t = T/2$, and $t = T$), indicating strong interactions between the two in that area.

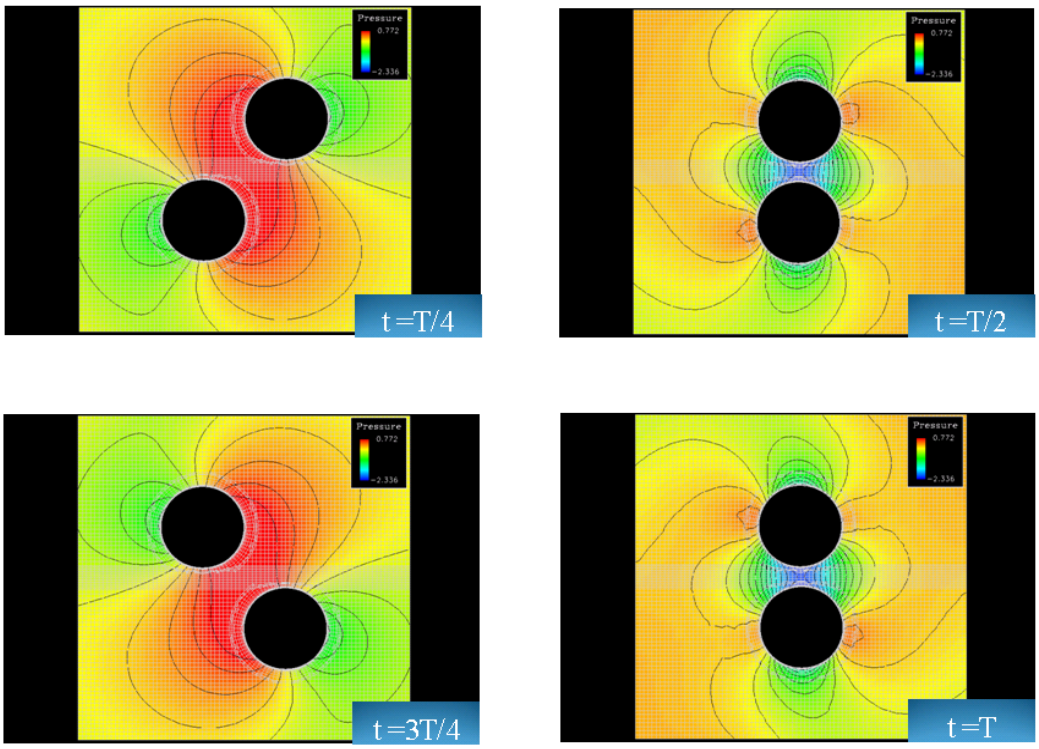

Figure 6.23: Pressure contours of two oscillating cylinders in one period.

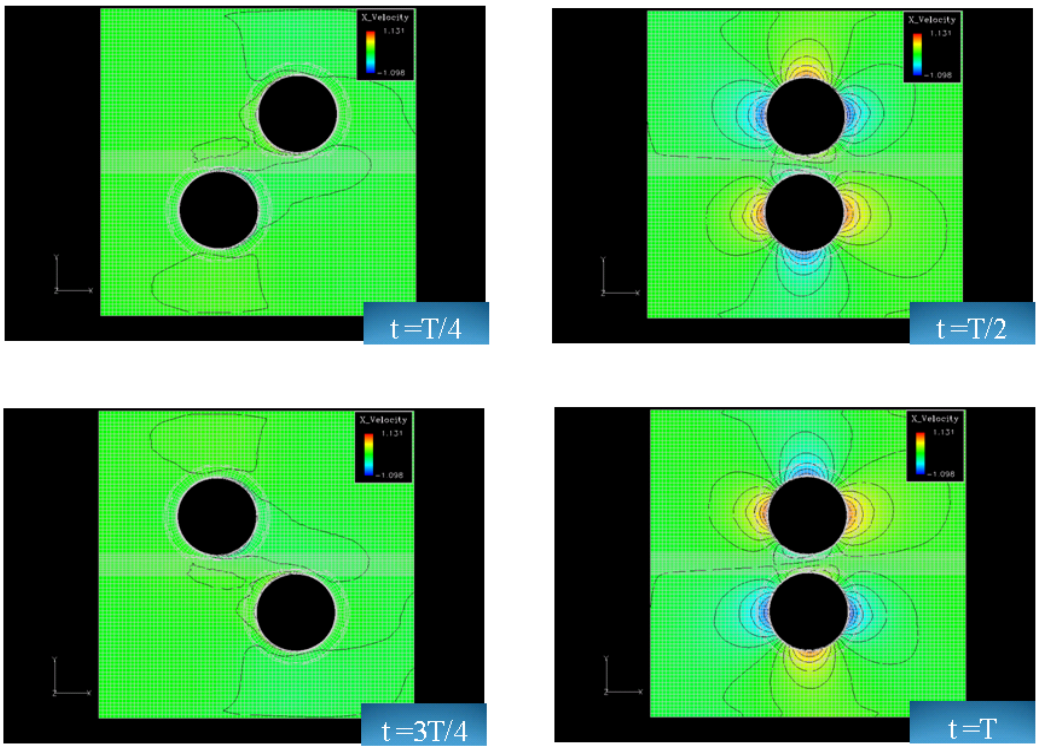

Figure 6.24: X-Velocity contours of two oscillating cylinders in one period.

6.4.2.3 Suboff Validation

Overset method is validated in an applicaiton of a static 3D Suboff in freestream. Half of a 3D Suboff geometry is used in the test. Mesh details of the symmetry plane are shown in Figure 6.25. With $Re = 12M$, the simulation results C_p and C_f compared with experiment data are shown in Figure 6.26 and Figure 6.27 with very good agreement.

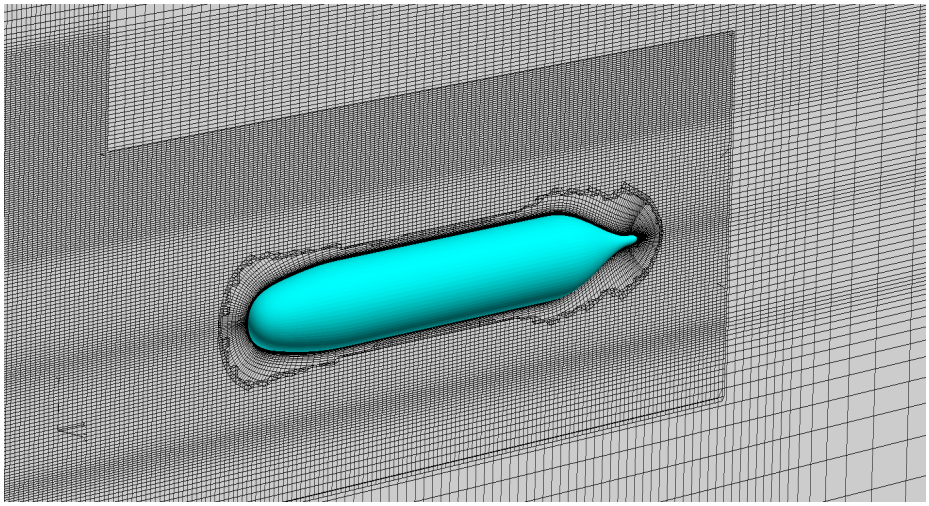

Figure 6.25: Mesh details of the Suboff at the symmetry plane.

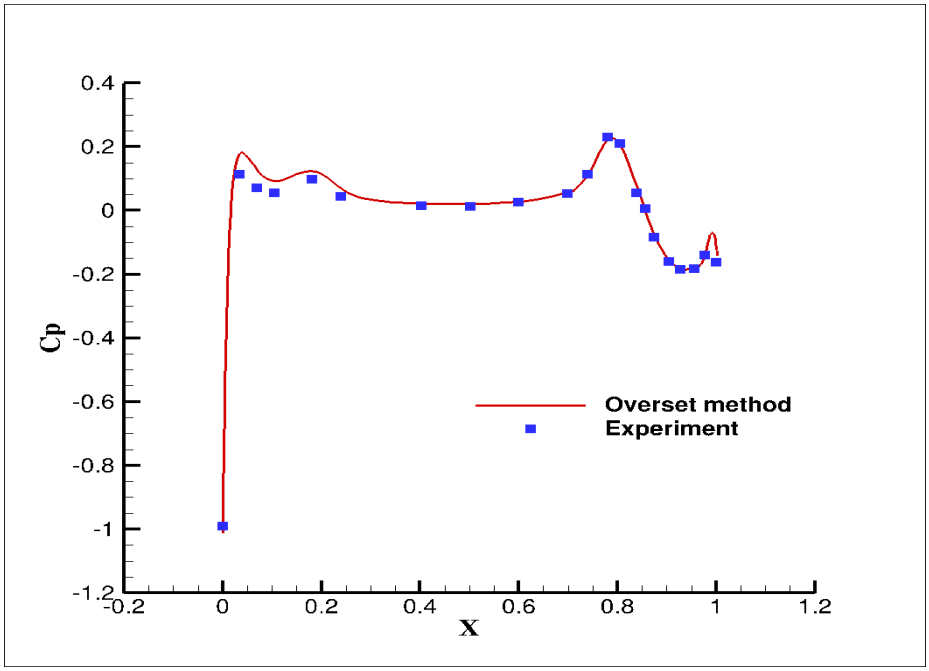

Figure 6.26: Comparison of C_p between overset method and experiment data.

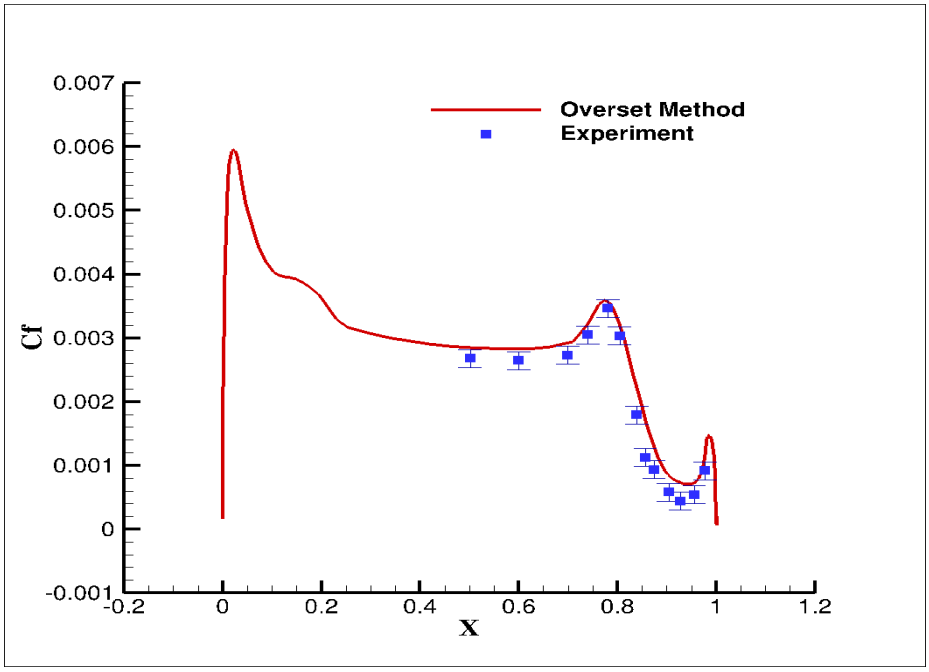

Figure 6.27: Comparison of C_f between overset method and experiment data with 5-percent uncertanty.

6.4.2.4 2D S175 Container Ship Interacting with Suboff

The motivation behind developing the overset grid method is mainly for handling multiple moving bodies in relative motion applications, especially for studying the interaction between an S175 container ship and a Suboff when they are passing each other at close distance. It is predicted that negative pressure generated bewteen these two could be large enough to pull them together, which might result in collision and cause safety issues for the crew members. So it is important to simulate this scenario and accurately predict the interaction between the ship and the Suboff. As the first step of research into this multi-year project, the motion of these two vehicles are prescribed, i.e., they are only allowed to move parallel in horizontal directions, and refrain from any other 6DOF motions. Two tests have been performed in still water and free-streaming conditions respectively.

First, the S175 container ship and the Suboff are placed in still water, separated far from each other in X direction and 0.2 body length of Suboff in Y direction. The container ship is set still and refrained from any motions, while the Suboff is moving toward the ship. The Suboff is accelerating from static mode first and then remaining uniform speed, as shown in the velocity profile from Figure 6.28.

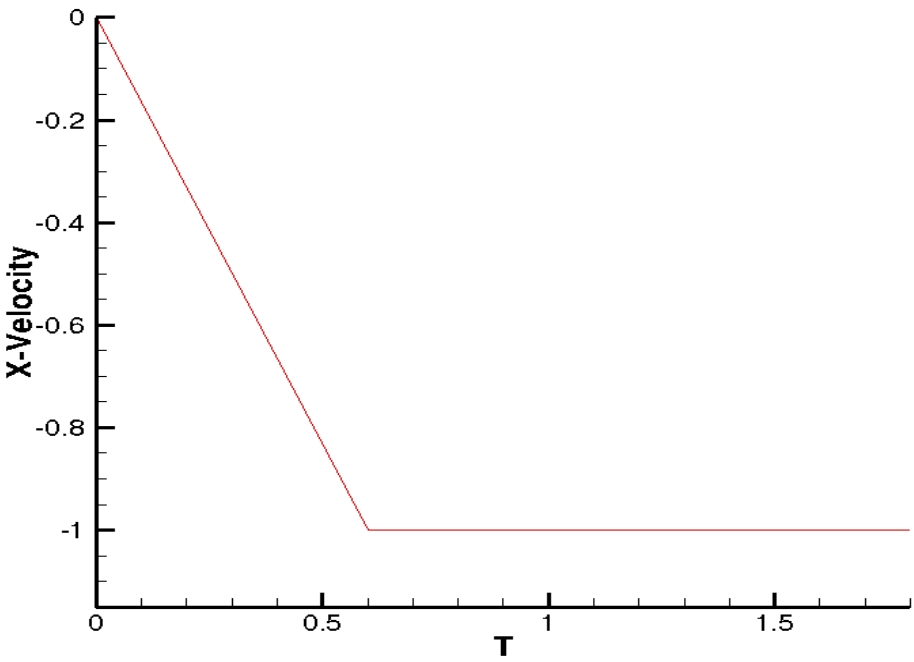

Figure 6.28: Velocity profile of the Suboff.

Overlap minimization is used to avoid large overlap between grids which is the source of inaccurate/non-smooth solutions. The assembled 2D overset grids after hole cutting are shown in Figure 6.29. Close-up views of the S175 ship with and without overlap minimization are shown in Figure 6.30 and 6.31 respectively, which indicates the overlap region between the ship grid and the background grid is significantly reduced; Close-up views of the Suboff with and without overlap minimization are shown in Figure 6.32 and 6.33. Utilizing overlap minimization on overset grids, unsteady flow solutions were obtained using Menter's SAS one equation model at $Re = 1e6$, with time step of $3e$-4. 6000 time steps were used in total run. The pressure contour evolution is shown from Figure 6.34. Strong interaction can be observed when the Suboff is passing beneath the ship, indicating the negative pressure that tends to draw the two vehicles together.

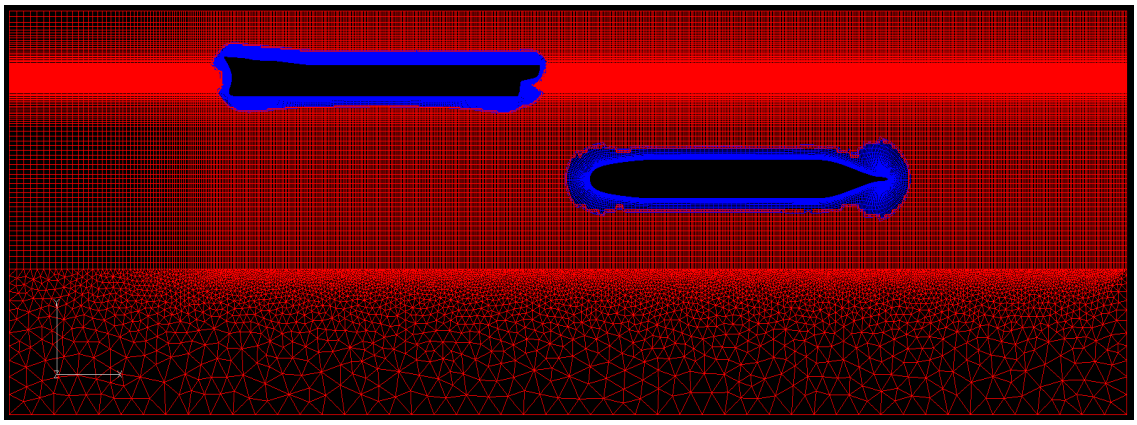

Figure 6.29: Assembled 2D overset grids after hole cutting for ship-Suboff interaction simulations; Red nodes indicate active points from the ship grid, and blue nodes indicate active points from the background grid.

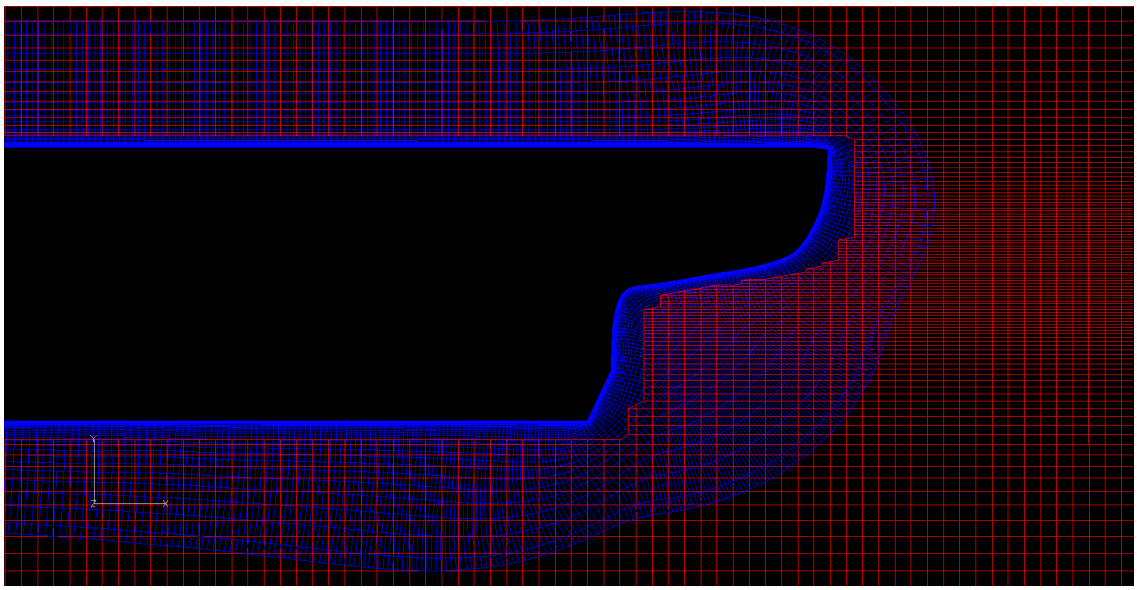

Figure 6.30: Assembled 2D overset grids after hole cutting for S175 ship without overlap minimization; Blue nodes indicate active points from the ship grid, and red nodes indicate active points from the background grid.

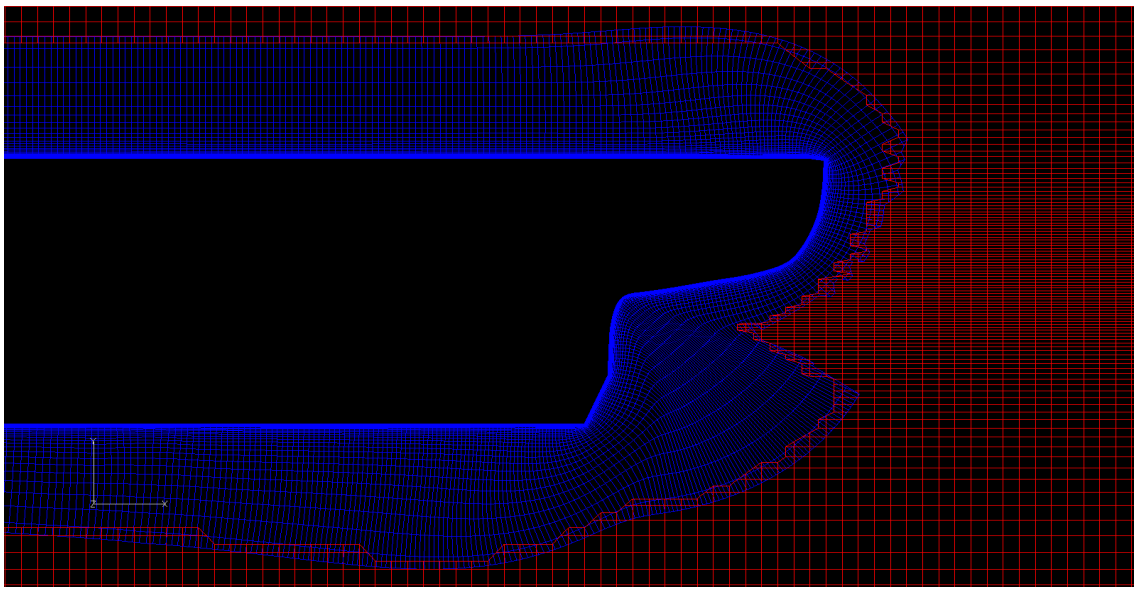

Figure 6.31: Assembled 2D overset grids after hole cutting for S175 ship with overlap minimization; Blue nodes indicate active points from the ship grid, and red nodes indicate active points from the background grid.

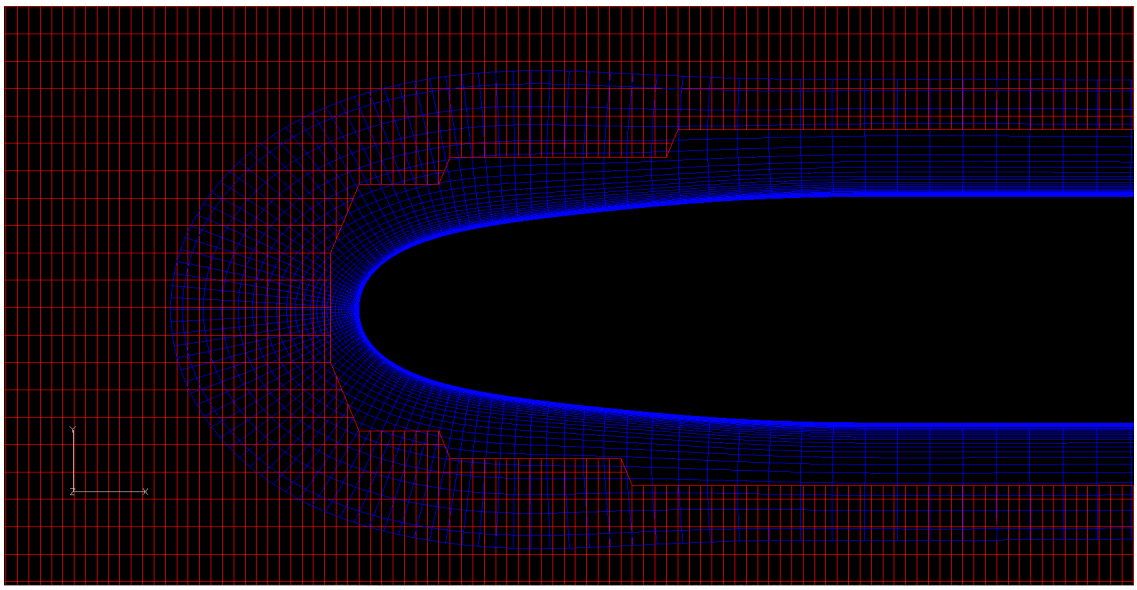

Figure 6.32: Assembled 2D overset grids after hole cutting for Suboff without overlap minimization; Blue nodes indicate active points from the Suboff grid, and red nodes indicate active points from the background grid.

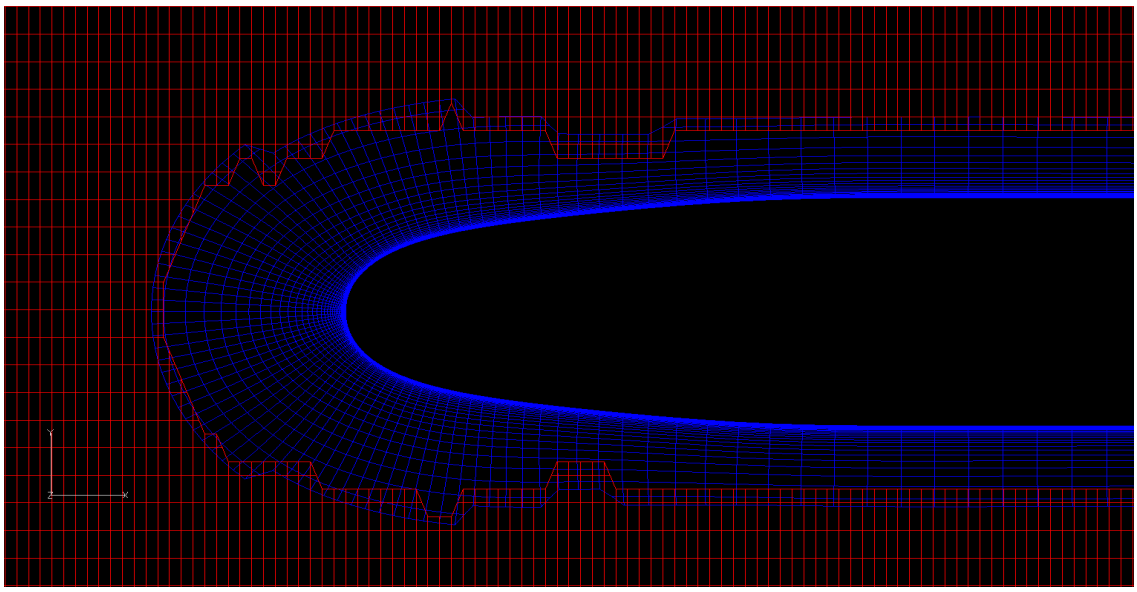

Figure 6.33: Assembled 2D overset grids after hole cutting for Suboff with overlap minimization; Blue nodes indicate active points from the ship grid, and red nodes indicate active points from the background grid.

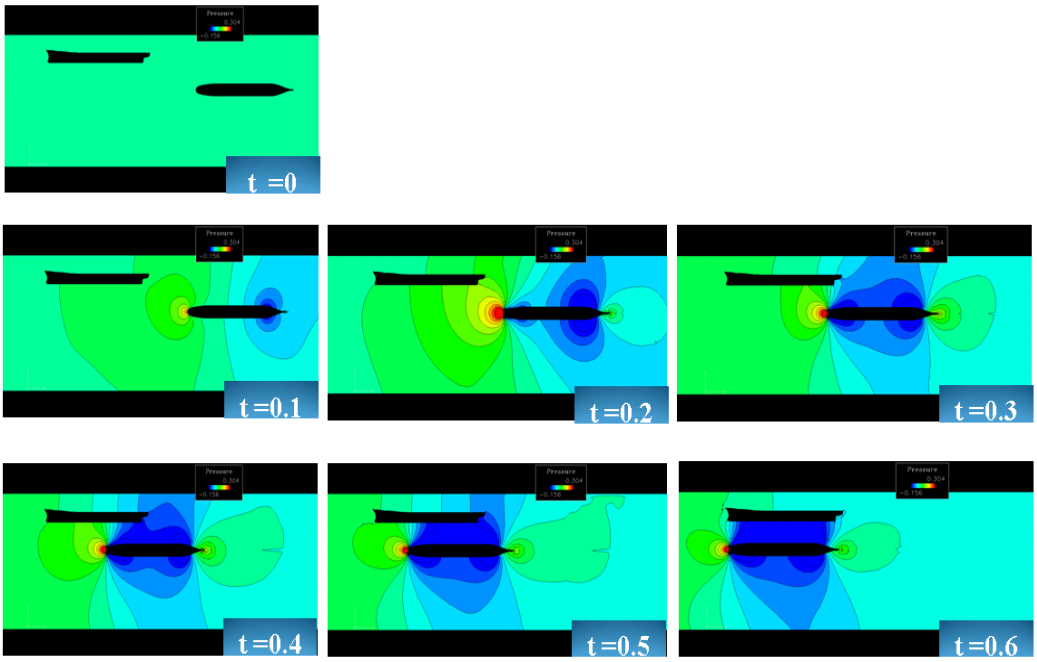

Figure 6.34: Pressure contour evolution of ship-suboff interaction in still water.

For the second test, the still water condition in the first test is now replaced by free stream against the advancing Suboff which also creates a turbulent boundary layer over the ship, and everything else is the same as the first one. Similar interaction between ship and Suboff can be observed from Figure 6.35.

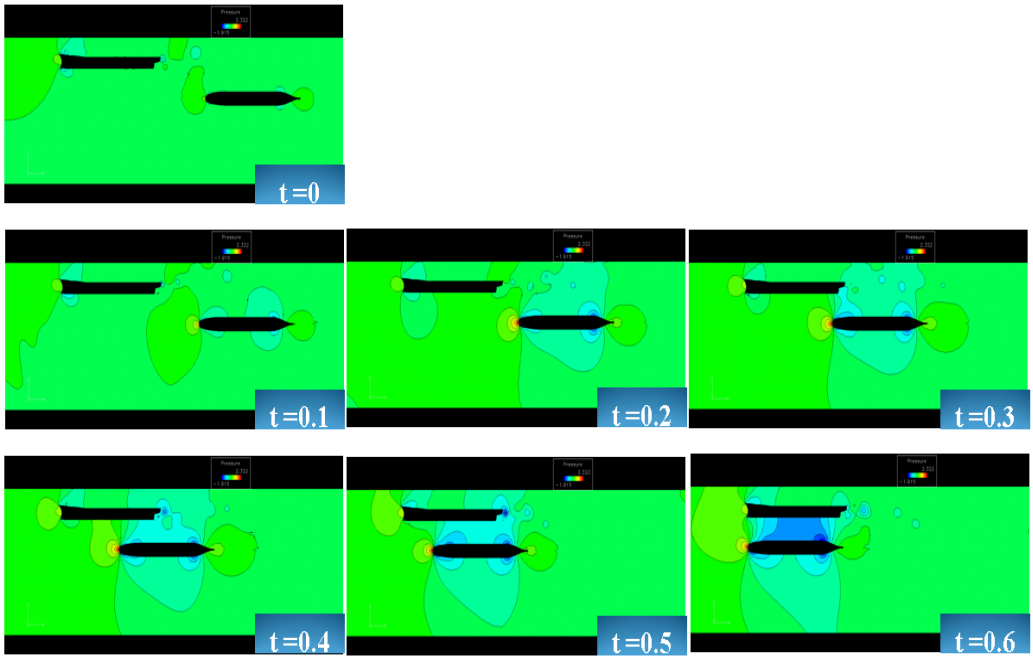

Figure 6.35: Pressure contour evolution of ship-suboff interaction in free stream.

6.4.2.5 3D S175 Container Ship Interacting with Suboff

After 2D overset grids are successfully tested, 3D grids are used to further test this overset approach and study the interaction. The geometric boundary layout of overset grids used is displayed in Figure 6.36. Body fitted grids are generated around the ship and Suboff. A refinement background grid with fine spacing is used locally in the interaction region of the two vehicles, while a coarse grid is also embedded as background. The mesh details of assembled 3D overset grids at the symmetry plane are shown in Figure 6.37. The pressure contour evolution is shown in Figure 6.38. The x-velocity contour evolution is shown in Figure 6.39.

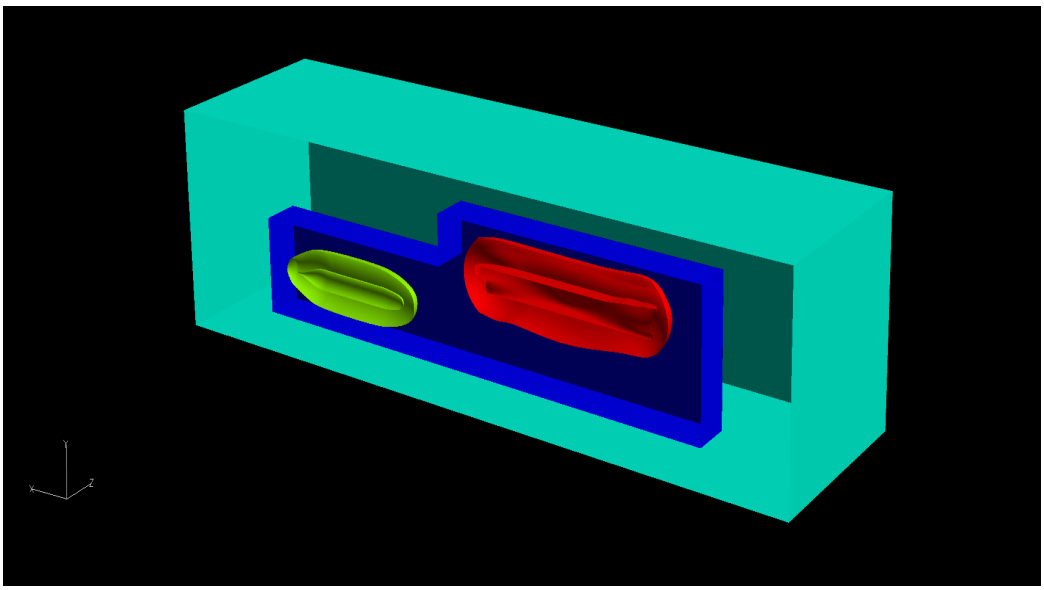

Figure 6.36: Geometric boundary layout of the 3D overset grids, including Suboff (yellow), S175 ship (red), fine background (blue), and coarse background (green).

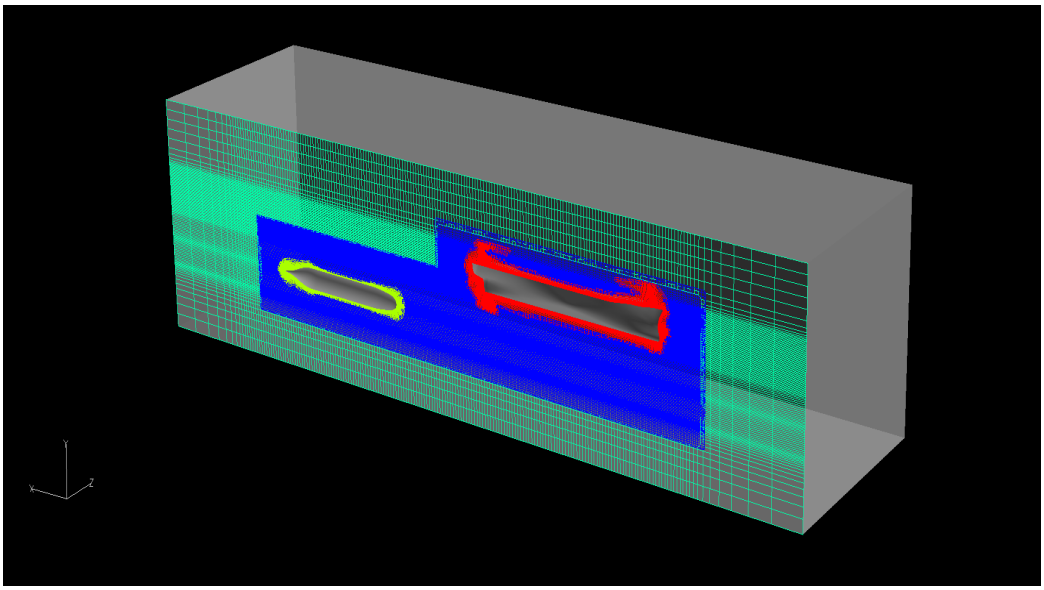

Figure 6.37: Highlight of the symmetry plane for the assembled 3D overset grids.

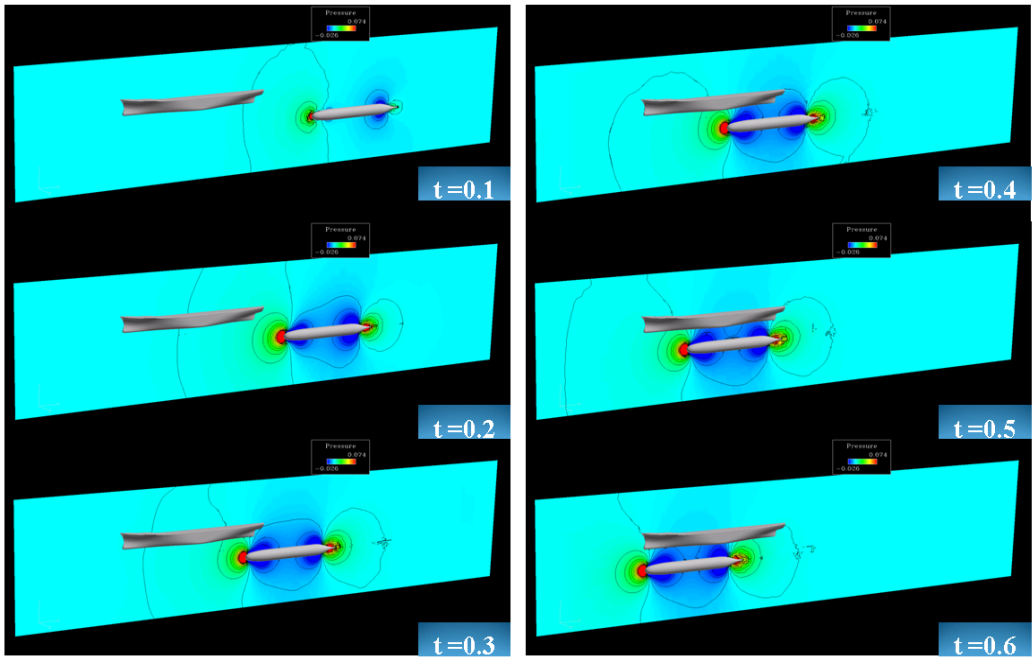

Figure 6.38: Pressure contour evolution of 3D ship-suboff interaction in still water.

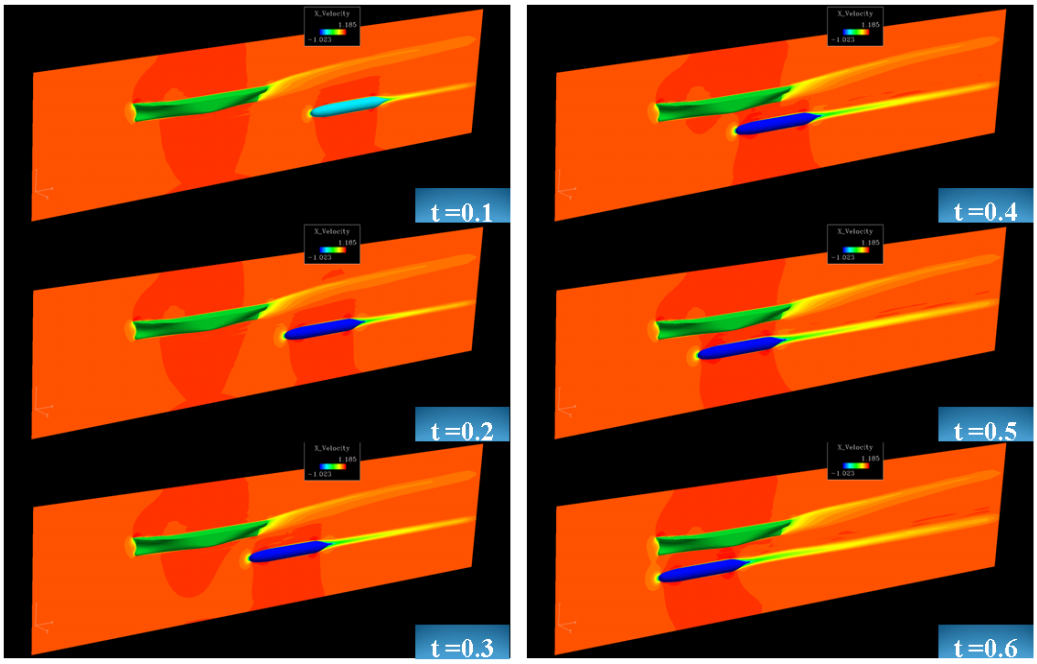

Figure 6.39: X-Velocity contour evolution of 3D ship-suboff interaction in free stream.

All the simulations above have shown the strong interaction between the ship and Suboff when they are passing each other. To quantitively show the large undesirable influence that the ship can put on Suboff, the comparison of lift on Suboff is studied between two cases: one with Suboff-ship interaction, and the other with only Suboff. For the Suboff isolation case, the lift is almost zero. However, for the Suboff-ship interaction one, the lift per square meter can be as high as 8.6 ambient pressure (860 kPa), which is large enough to pull the Suboff and ship together. This means that the dramtic change of lift on the Suboff during the interaction with the ship can cause safety issues for the crew members as predicted. More simulations, including a comparison against experiment, will be investigated as more data from the project sponsors become available.

6.5 Running Time Comparison of Different Mesh Movement Schemes

In order to study the efficiency of different mesh movement schemes, an oscillating cylinder simulation was tested using rigid motion method, overset grid method, AIM method, and PDE method. The same 2D grid configurations used for comparison between rigid motion and overset grid methods before were used. A single grid with $29,040$ nodes was used for all the non-overset methods. With the same conditions (oscillating function, time step, etc.), the averaged running time comparison for each time step is shown in Figure 6.40. Not surprisingly, the rigid motion method is the most efficient. Overset grid method is quite efficient, given that the grids used in this test has $126,243$ nodes which is almost 4 times of the single grid. The AIM method is much cheaper than the PDE method, which justifies the choice of choosing AIM over PDE for the unsteady hydrodynamic simulations in this work.

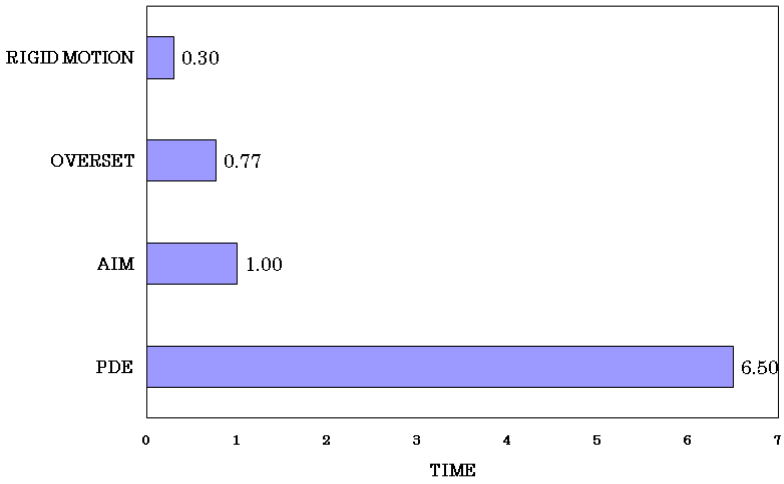

Figure 6.40: Running time comparison of different mesh movement methods. All the running time is scaled based on the AIM method.

Chapter 7

CONCLUSIONS AND FUTURE WORK

Unstructured grid technologies are developed and implemented into the *Tenasi* flow solver to manage complex unsteady simulations for deforming grids and relative motions. These capabilitis are added in response to the SimCenter project requirements allowing simulations for objects with large relative motion and close proximity.

A parallel universal mesh deformation scheme is developed and presented to manage deforming surface and volume grids for both aerodynamic and hydrodynamic applications. The approach is universal and independent of grid type; structured or unstructured. Also, it requires minimal inter-processor communication and is thus perfectly suitable to a parallel platform. The original scheme of Allen (2006) has difficulty deforming volume grids in regions near concave geometry features and for abrupt grid resolution changes. Several modifications are proposed to overcome these problems. Grid quality can be improved significantly by adding a smoothing algorithm and additional surface mesh connectivity. The mesh deformation scheme is demonstrated and validated by solutions of several synthetic jet test cases from a NASA Langley Workshop. Application to the free surface flow over the

S175 container ship undergoing two-node harmonic bending was also demonstrated. The resulting viscous mesh shows good quality throughout the harmonic deformation with large scale vortex shedding occurring at the bow and stern.

Overset grid technology is adopted to simulate the flow past multiple moving bodies in relative motion. DiRTlib and SUGGAR developed by Noack (2005) is used to facilitate integration of the overset grid method into the *Tenasi* flow solver. First, simulation of an oscillating cylinder using overset grids is compared with a baseline configuration using a single grid in rigid motion (i.e., no relative motion between the cylinder and the farfield) with excellent agreement. Then interaction between two oscillating cylinders with the same amplitude and frequency but 180-degree phase difference is studied. Finally, as the primary motivation for developing a simulation capability for modeling the dynamics of interacting platforms, a Suboff passing beneath a container ship is simulated using both 2D and 3D overset grids, and satisfactory results are obtained. Dynamic overset approach has been proved to be a viable option for simulations with large relative motion and close proximity.

Future work includes using the improved AIM to perform fully coupled simulations for the container ship in incident waves by tightly coupling the *Tenasi* flow solver with a finite element solver to predict the vibration response due to slamming. In-house overset capability is desirable for improved flexibility, support, and customization for project needs, while the current work can certainly provide knowledge base and foundation for such technologies. The Overset grid approach will be used to validate the ship-Suboff interaction case as experiment data from the project sponsors become available. Also, it will be further validated against a store separation application in predicting trajectory characteristic at transonic speeds.

Bibliography

[1] Allen, C.B., "Flow-Solver and Mesh Motion Scheme for Forward Flight Rotor Simulation," 24th Applied Aerodynamics Conference, Sanfrancisco, California, 2006.

[2] Anderson, W. K., and Bonhaus, D. L., "An Implicit Upwind Algorithm for Computing Turbulent Flows on Unstructured Grids," Computers and Fluids, 23(1), pp. 1-21, 1994.

[3] Atsavapranee, P., Miller, R., Dai, C., Klamo, J, and Fry, D., "Steady-Turning Experiments and RANS Simulations on a Surface Combatant Hull Form (Model #5617)," 28th ONR Symposium on Naval Hydrodynamics, Pasadena, California, Sep. 2010.

[4] Batina, J.T., "Unsteady Euler Airfoil Solutions Using Unstructured Dynamic Meshes," AIAA Journal 28(8), pp. 1381-1388, 1990.

[5] Benek, J.A., Steger, J., and Dougherty, F., "A Flexible Grid Embedding Technique with Applications to the Euler Equations," AIAA Paper 83-1944, 1983.

[6] Betts, C.V., Bishop, R.E.D., and Price, W.G., "The Symmetric Generalized Fluid Forces Applied to a Ship in a Seaway," Transactions of the Royal Institution of Naval Architects 199, pp. 265-278, 1977.

[7] Bishop, R.E.D., and Price, W.G., "The Generalised Antisymmetric Fluid Forces Applied to a Ship in a Seaway," International Shipbuilding progress 24, pp. 3-14, 1977.

[8] Bishop, R.E.D., and Price, W.G., Hydroelasticity of Ships. Cambridge University Press, London, UK, 1979.

[9] Broglia, R., and Iafrati, A., "Hydrodynamics of Planing Hull in Asymmetric Conditions," 28th ONR Symposium on Naval Hydrodynamics, Pasadena, California, Sep. 2010.

[10] Broglia, R., Muscari, R. and Di Mascio, A., "Numerical Analysis of Blockage Effects in PMM Tests," Proceedings of the 26th ONR Symposium on Naval Hydrodynamics, Rome, Italy, 2006.

[11] Carrica, P., Wilson, R., and Stern, F., "Unsteady RANS Simulation of the Ship Forward Speed Diffraction Problem," Computers and Fluids 35, pp. 545-570, 2006.

[12] Carrica, P., Wilson, R., Noack, R., and Stern, F., "Ship Motions Using Single-Phase Level Set with Dynamic Overset Grids," Computers and Fluids 36(9), pp. 1415-1433, 2007.

[13] Chen, X.J., Wu, Y.S., Cui, W.C., and Jensen, J.J., "Review of Hydroelasticity Theories for Global Response of Marine Structures," Ocean Engineering 33, pp. 439-457, 2006.

[14] Chorin, A.J., "A Numerical Method for Solving Incompressible Viscous Flow Problems," Journal of Computational Physics 2, pp. 12-26, 1967.

[15] Cook, R.D., Finite Element Modeling for Stress Analysis. John Wiley & Sons, Inc., New York, 1995.

[16] Cui, J., and Agarwal, R.K., "3D CFD Validation of a Synthetic Jet in Quiescent Air (NASA Langley Workshop Validation: Case 1)," AIAA Paper 2004-2222, 2004.

[17] Dreyer, J.J., and Boger, D.A., "Validation of a Free-Swimming, Guided Multibody URANS Simulation Tool," 28th ONR Symposium on Naval Hydrodynamics, Pasadena, California, Sep. 2010.

[18] Durante, R., Broglia, R., Muscari, R., and Di Mascio, A., "Numerical simulations of a turning circle manoeuvre for a fully appended hull," 28th ONR Symposium on Naval Hydrodynamics, Pasadena, California, Sep. 2010.

[19] Faltinsen, O., and Zhao, R., "Numerical Prediction of Ship Motions at High Forward Speed," Philosophical Transactions of the Royal Society of London, Series A 334, pp. 241-252, 1991(a).

[20] Faltinsen, O., and Zhao, R., "Flow Predictions Around High-Speed Ships in Waves. Mathematical Approaches in Hydrodynamics," Society for Industrial and Applied Mathematics, pp. 265-288, 1991(b).

[21] Farhat, C., Degand, C., Koobus, B., and Lesoinne, M., "Torsional Springs for Two-Dimensional Dynamic Unstructured Fluid Meshes," Comput. Methods Appl. Mech. Engrg 163, pp. 231-245, 1998.

[22] He, J.M., and Fu, Z.F., Modal Analysis. 2nd edition. Butterworth-Heinemann, MA, USA, 2001.

[23] Heller, S.R., and Abramson, H.N., "Hydroelasticity: a New Naval Science," Journal of America Society of Naval Engineers 71(2), pp. 205-209, 1959.

[24] Hermundstad, O.A., "Theoretical and Experimental Hydorelastic Analysis of High Speed Vessels," Ph.D. Thesis, Dept. Marine Structures. Norwegian University of Science and Technology, 1995.

[25] Hermundstad, O.A., Aarsns, J.V. and Moan, T., "Linear Hydroelastic Analysis of High-Speed Catamarans and Monohulls," Journal of Ship Research 43(1), pp. 48-63, 1999.

[26] Hermundstad, O.A., "Springing and Whipping of Ships," Lecture notes in Hydroelasticiy, 2007.

[27] Hino, T., "Proceedings of CFD Workshop Tokyo 2005," National Maritime Research Institute, Tokyo, Japan, 2005.

[28] Hochbaum, A., "Virtual PMM Tests for Maneuvering Prediction," Proceedings of the 26th ONR Symposium on Naval Hydrodynamics, Rome, Italy, Sep. 2006.

[29] Hochbaum, A., and Vogt, M., "Towards the Simulation of Seakeeping and Maneuvering Based on the Computation of the Free Surface Viscous Flow," Proceedings of the 24th ONR Symposium on Naval Hydrodynamics, Fukuoka, Japan, 2002.

[30] Huerta, A., and Liu, W.K., "Viscous Flow Structure Interaction," Journal of Pressure Vessel Technology 110, pp. 15-21, 1988.

[31] Hyams, D.G., "An Investigation of Parallel Implicit Solution Algorithm for Incompressible Flow on Unstructured Topologies," Ph.D. Disseration, Mississippi State University, May 2000.

[32] Jensen, J.J., and Dogliani, M., "Wave-Induced Ship Hull Vibrations in Stochastic Seaways," Marine Structures 9(3), pp. 353-387, 1996.

[33] Jensen, J.J. and Pedersen, P.T., "Wave-Induced Bending Moments in Ships–a Quadratic Theory," Transactions of the Royal Institution of Naval Architects 121, pp. 151-165, 1979.

[34] Journée, J.M.J., "Experiments and Calculations on Four Wigley Hullforms. Delft University of Technology," Ship Hydrodynamic Laboratory, Report No. 909, 1992.

[35] Karman, S.L.Jr., and Sahasrabudhe, M., "Unstructured Adaptive Elliptic Smoothing," AIAA Paper 2007-0559, 2007.

[36] Koomullil, R., Cheng, G., Soni, B., Noack, R., and Prewitt, N., "Moving-Body Simulations Using Overset Framework with Rigid Body Dynamics," Mathematics and Computers in Simulation 78, pp. 618-626, 2008.

[37] Korvin-Kroukovsky, V.B. and Jacobs, W.R., "Pitching and Heaving Motions of a Ship in Regular Waves," Transactions of The Society of Naval Architects and Marine Engineers (SNAME) 65, pp. 590-632, 1957.

[38] Larson, L., Stern, F. and Bertram, V., Benchmarking of Computational Fluid Dynamics for Ship Flows: the Gothenburg 2000 Workshop. Journal of Ship Research 47(1), pp. 63-81, 2003.

[39] Larson, L., Stern, F., and Bertram, V. (Editors), "Gothenburg 2000: A Workshop on Numerical Hydrodynamics," Department of Naval Architecture and Ocean Engineering, Chalmers University of Technology, Gothenburg, Sweden, 2002.

[40] Lee, D., Maki, K., Wilson, R., Troesch, A., and Vlahopoulos, N., "Dynamic Response of a Marine Vessle Due to Wave-Induced Slamming," Lecture Notes in Applied and Computational Mechanics 44, pp. 161-172, 2009.

[41] Löhner, R. and Yang, C., Improved ALE Mesh Velocities for Moving Bodies, Communications in Numerical Methods in Engineering 12, pp. 599-608, 1996.

[42] Madrane, A., Raichle, A., and Stuermer, A., "Parallel Implementation of a Dynamic Unstructured Chimera Method in the DLR Finite Volume TAU-Code," 12th Annual Conference of the CFD Society of Canada, Ottawa, Ontario, Canada, pp.524-534, 2004.

[43] Miller, R., and Kim, S.E., "A Computational Framework for Fluid-Structure Interaction on Flexible Propellers Involving Large Deformation," 28th ONR Symposium on Naval Hydrodynamics, Pasadena, California, Sep. 2010.

[44] Moctar, O., Schellin, T., and Priebe, T., "CFD and FE methods to Predict Wave Loads and Ship Structural Response," 26th Symposium on Naval Hydrodynamics, Rome, Italy, Sep. 2006.

[45] Muscari, R., Felli, M., and Di Mascio, A., "Numerical and experimental analysis of the flow around a propeller behind a fully appended hull," 28th ONR Symposium on Naval Hydrodynamics, Pasadena, California, Sep. 2010.

[46] Nakahashi, K., Togashi, F., and Sharov, D., "Intergid-Boundary Definition Method for Overset Unstructured Grid Approach," AIAA J. 38(11), pp.2077-2084, 2000.

[47] Nichols, D.S., "Development of a Free Surface Method Utilizing an Incompressible Multi-Phase Algorithm to Study the Flow About Surface Ships and Underwater Vehicles," Ph.D Dissertation, Mississippi State University, Aug. 2002.

[48] Noack, R.W., "DiRTlib: A Library to Add an Overset Capability to Your Flow Solver," 17th AIAA Computational Fluid Dynamics Conference, AIAA Paper 2005-5116, Toronto, Ontario, Canada, June 2005(a).

[49] Noack, R.W., "SUGGAR: A General Capability for Moving Body Overset Grid Assembly," 17th AIAA Computational Fluid Dynamics Conference, AIAA Paper 2005-5116, Toronto, Ontario, Canada, June 2005(b).

[50] Orihara, H., and Miyata, H., "Evaluation of Added Resistance in Regular Incident Waves by Computations Fluid Dynamics Motion Simulation Using Overlapping Grid System," Journal of Marine Science and Technology 8, pp. 47-60, 2003.

[51] Orych, M., Larson, L., and Regnström, B., "Adaptive overlapping grid techniques and spatial discretization schemes for increasing surface sharpness and numerical accuracy in free surface capturing methods," 28th ONR Symposium on Naval Hydrodynamics, Pasadena, California, Sep. 2010.

[52] Pandya, M.J., Frink, N.T., and Noack, R.W., "Progress Toward Overset-Grid Moving Body Capability for USM3D Unstructured Flow Solver," 17th AIAA Computational Fluid Dynamics Conference, Toronto, Ontario, Canada, June 2005.

[53] Ramamurti, R., Löhner, R., and Sandberg, W.C., "Computation of the 3-D unsteady flow past deforming geometries," Int. J. Comp. Fluid Dyn. 13, pp. 83-99, 1999.

[54] Ramos, J., Incecik, A., and Guedes Soares, C., "Experimental Study of Slam-Induced Stresses in a Container Ship," Marine Structures, 13, pp. 25-51, 2000.

[55] Regnström, B., and Bathfield, N., "Drag and Wake Prediction for Ships with appendages using an overlapping grid method, " 26th Symposium on Naval Hydrodynamics, Rome, Italy, Sep. 2006.

[56] Roe, P. L., "Approximate Riemann Solvers, Parameter Vectors, and Difference Schemes," J. Comp. Phys. 43, pp. 357-372, 1981.

[57] Rumsey, C.L., "Successes and Challenges for Flow Control Simulations," AIAA Paper 2008-4311, 2008.

[58] Rumsey, C.L., Gatski, T.B., Sellers, W.L., Vatsa, V.N., and Viken, S.A., "Summary of the 2004 CFD Validation Workshop on Synthetic Jets and Turbulent Separation Control," AIAA Paper 2004-2217, 2004.

[59] Salvesen, N., Tuck, E.O. and Faltinsen, O., "Ship Motions and Sea Loads," Transactions of SNAME 78, pp. 250-287, 1971.

[60] Singh, S.P., and Sen, D., "A Comparative Linear and Nonlinear Ship Motion Study Using 3-D Time Domain Methods," Ocean Engineering 34, pp. 1863-1881, 2007.

[61] Suhs, N., Rogers, S., and Dietz, W., "PEGASUS 5: An Automated Pre-processor for Overset-Grid CFD," AIAA Paper 2002-3186, 2002.

[62] Taylor, L. K., "Unsteady Three-Dimensional Incompressible Algorithm Based on Artificial Compressibility," Ph.D. Dissertation, Mississippi State University, 1991.

[63] Wilson, R.V., Nichols, D.S., Mitchell, B., Karman, S.L.Jr., Hyams, D.G., Sreenivas, K., Taylor, L.K., Briley, W.R., and Whitfield, D.L., "Application of an Unstructured Free Surface Flow Solver for High Speed Transom Stern Ships," 26th Symposium on Naval Hydrodynamics, Rome, Italy, Sep. 2006(a).

[64] Wilson, R.V., Carrica, P.M., and Stern, F., "URANS Simulations for a High-Speed Transom Stern Ship with Breaking Waves," International Journal of Computational Fluid Dynamics 20(2), pp. 105-125, 2006(b).

[65] Wilson, R.V., Carrica, P.M., and Stern, F., "Unsteady RANS Method for Ship Motions with Application to Roll for a Surface Combatant," Computers & Fluids 35, pp. 501-524, 2006(c).

[66] Wilson, R., Nihcols, S., Mitchell, B., Karman, S., Betro, V., Hyams, D., Sreenivas, K., Taylor, L., Briley, R., and Whitfield, D., "Simulation of a Surface Combatant

with Dynamic Ship Maneuvers," 9th International Conference in Numerical Ship Hydrodyanmics, University of Michigan, Aug. 2007.

[67] Wilson, R.V., Ji, L., Karman, S.L.Jr., Hyams, D.G., Sreenivas, K., Taylor, L.K., Briley, W.R., and Whitfield, D.L., 2008. Simulation of Large Amplitude Ship Motions for Prediction of Fluid-Structure Interaction. Proceedings of the 27th ONR Symposium on Naval Hydrodynamics, Seoul, Korea, Oct. 2008.

[68] Wilson, R.V., "A Review of Computational Ship Hydrodynamics," 2008.

[69] Wu, M.K., and Moan, T., "Linear and Nonlinear Hydroelastic Analysis of High-Speed Vessels," Journal of Ship Research 40(2), pp. 149-163, 1996.

[70] Xia, J.Z., Wang, Z.H., and Jensen, J.J., "Non-Linear Wave Loads and Ship Responses by a Time-Domain Strip Theory," Marine structures 11(3), pp. 101-123, 1998.

[71] Xia, H., and Qin, N., "Dynamic Grid and Unsteady Boundary Conditions for Synthetic Jet Flow," AIAA Paper 2005-106, 2005.

[72] Yammamoto, Y., Iida, K., Fukasawa, T., Murakami, T., Arai, M., and Ando, A., Structural Damage Analysis of a Fast Ship Due to Bow Flare Slamming. International Shipbuilding Progress 32, pp. 124-136, 1985.

[73] Yang, C.I., and Moran, T.J., "Finite-Element Solution of Added Mass and Damping of Oscillation Rods in Viscous Fluids," Journal of Applied Mechanics 46, pp. 519-523, 1979.

[74] Yao, C.S., Chen, F.J., and Neuhart, D., "Synthetic Jet Flowfield Database for Computational Fluid Dynamics Validation," AIAA Journal 44(12), pp. 3153-3157, 2006.

Vita

Lei Ji was born to Fengting Ji and Guizhi Li in Chifeng, China on June 26, 1982. He was raised in Jinshan, a small town of Chifeng, and went to high school there. He graduated from Jinshan Middle School in 2000. From there, he went to the Dalian University of Technology and received a B.S. in Thermal Engergy and Power Engineering in 2004. He came to US to pursue his graduate degree after graduation. He graduated from the University of Nebraska–Lincoln for M.S. in Mechanical Engineering. Lei is going to graduate with his Ph.D degree in Computational Engineering at the University of Tennessee at Chattanooga in May 2011. He hopes to continue his research on fluid-structure interaction methods and applications in the future.